Ore Geology Reviews 168 (2024) 106068

Contents lists available at ScienceDirect

Ore Geology Reviews

journal homepage: www.elsevier.com/locate/oregeorev

Novel comprehensions of lithological and structural features gleaned via Sentinel 2 texture analysis

Ali Shebl [a,b,*], Mohamed Badawi [c,d], Maher Dawoud [e], Mohamed Abd El-Wahed [b], Hanna A. El-Dokouny [e], Árpád Csámer [a,f]

[a] Department of Mineralogy and Geology, Faculty of Science and Technology, University of Debrecen, Egyetem tér 1, 4032 Debrecen, Hungary
[b] Department of Geology, Tanta University, 31527 Tanta, Egypt
[c] Institute of Exploration Geosciences, University of Miskolc, Miskolc, 3515 Hungary
[d] Department of Geology, Mansoura University, 35516 Mansoura, Egypt
[e] Department of Geology, Faculty of Science, Menoufia University, Egypt
[f] Cosmochemistry and Cosmic Methods Research Group, University of Debrecen, Debrecen, 4032, Hungary

ARTICLE INFO

Keywords:
Remote sensing
Sentinel 2
Geological mapping
Co-occurrence Matrix
Eastern desert

ABSTRACT

Detailed geological mapping is the decisive key for mineral deposit prospecting, deciphering tectonic models, and outlining the main framework for most development programs and constructions. Without a doubt, various remote sensing datasets have introduced reliable lithological and structural mapping solutions. The main defect with remote sensing data is the curse of dimensionality, especially with hyperspectral data, where a lot of time is spent handling and selecting representative bands for various geological analyses. Consequently, and for the first time, our research is an attempt to resolve the complicated structural patterns (lineaments, folds, foliations, and cross-cutting relationships) and enhance lithological discrimination using a single band (of Sentinel 2 and ALOS PRISM data) and textural analysis. Through several trials over different pixel sizes (2.5 m and 10 m) and various kernels (3×3, 7×7, or 11×11), reasonable results are obtained, enabling lithological discrimination, in-depth structural analysis (foliations, faults, joints, and folds), shape recognition of systematic rock bodies, and delineation of quaternary deposits using single band analysis rather than time-consuming multiple band processing. Our results have been verified using intensive fieldwork and accurate visual interpretations using different datasets (e.g., previous geological maps, remote sensing data, etc.). Upon field verification and petrographical investigations of this research outcomes, we strongly recommend the adopted approach for the geological community, as it opens the doors for various applications utilizing single-band second-order statistics. We expect that this research could significantly help the geological community by reviving several previous studies and being applicable for future research, besides offering a reasonable approach for minimizing the time and efforts required for detailed field studies by highlighting micro- and mesoscale structures.

1. Introduction

Due to its wide coverage (compared to conventional fieldwork) and low-cost, optical remote sensing data has increasingly been utilized in lithological mapping (Abd El-Wahed et al., 2019; Abdelkader et al., 2022; Badawi et al., 2022; Mu et al., 2023; Qiu et al., 2015b, 2024). Identification of various lithological units depends mainly on different mineralogical spectral signatures, which in turn are a representation of unique absorption and reflection characteristics depending on chemical composition, grain size, and texture (Carli and Sgavetti, 2011; Mu et al., 2020; Zaini et al., 2012). In various applications, including but not limited to lithological mappings, it is a tedious process to specify the pure spectral signature of image constituents, especially in complicated terrains where weathering, hydrothermal alterations, complicated structures (e.g., shear zones), and flash flooding mostly alter the spectral response of the rock units. This spectral mixing leads in most cases to misinterpretation that could affect the target of several researches. For instance, the well-known Si-O vibrational bond spectral characteristic is affected by the silica content, and the grain size mostly influences the characteristic spectral depth (Lyon, 1965). Furthermore, one of the main

* Corresponding author at: Department of Mineralogy and Geology, Faculty of Science and Technology, University of Debrecen, Egyetem tér 1, 4032 Debrecen, Hungary.
E-mail address: ali.shebl@science.tanta.edu.eg (A. Shebl).

https://doi.org/10.1016/j.oregeorev.2024.106068
Received 29 March 2023; Received in revised form 1 May 2024; Accepted 3 May 2024
Available online 7 May 2024

disadvantages of remote sensing data is its dimensionality (especially with hyperspectral data), which requires time and effort for handling datasets to get the desired information based on the application target. Additionally, several studies highlighted the deficiency of optical datasets in extracting linear features when compared to DEMs or Radar data.

To overcome these three constraints, several studies have used different kinds of datasets instead of or in addition to optical data. These include aeromagnetic data (Eldosouky and Elkhateeb, 2018), Phased Array type L-band Synthetic Aperture Radar-2 (PALSAR-2) (Ghosh et al., 2022), Dual-Pol Sentinel-1 Data (Lu et al., 2021), airborne thermal infrared (TIR) data (Kirkland et al., 2002; Vaughan et al., 2005), integrated multispectral and radiometric data (Harris, 1989; Shebl et al., 2021), combined multispectral datasets (Ahmadirouhani et al., 2018; Pour et al., 2018; Shebl et al., 2022; Shebl and Csámer, 2021a), and blended radar and optical sensors with DEMs (Lu et al., 2021; Qiu et al., 2015a; Shebl and Csámer, 2021a) to deliver accurate lithological and structural mapping.

However, despite its limitations, optical remote sensing data is still indispensable and commonly used in different applications due to its accessibility and handling ease compared to the previously mentioned other datasets. Consequently, this research is an attempt to resolve their main limitations through implementing the inherited textural characteristics of the multispectral datasets instead of the frequently utilized spectral-based lithological discrimination. Textural attributes are

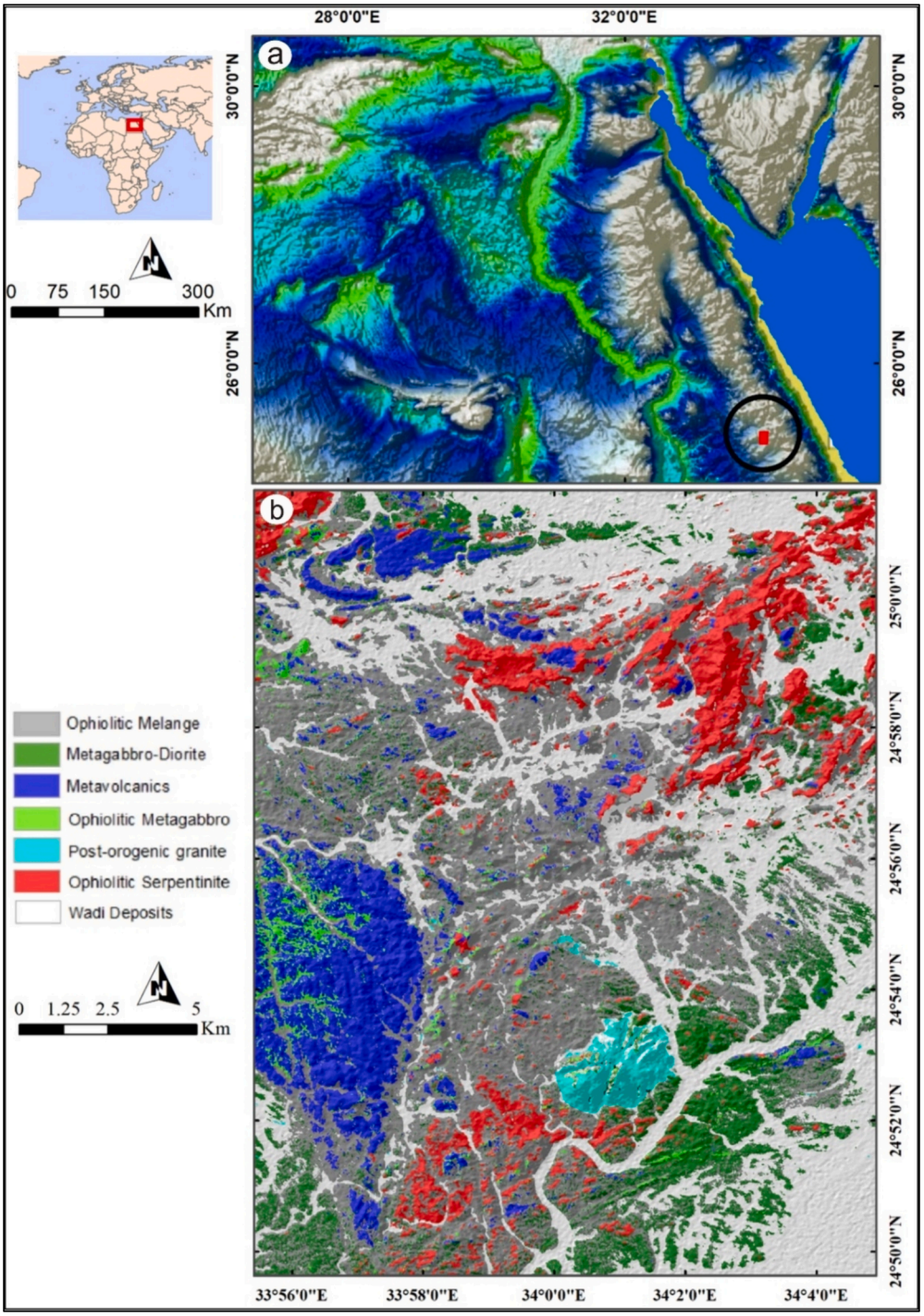

Fig. 1. (a) Location map of the study area. (b) Lithological map of the study area, modified after (Shebl et al., 2022; Zoheir et al., 2019).

mainly profound and comprise much deeper information compared to surface visual representations. These textural characteristics are supposed to be unique for each rock type, or generally any land cover, introducing a good solution for detailed lithological and structural mapping based on rigorous geological interpretation. Additionally, and based on different pixel intensities, edges including lineaments, foliation, and several structural features could be detected and delineated. To avoid data dimensionality, an informative single band is utilized to decipher the lithological and structural characteristics of the study area (the Mueilha area and its environs as a case study from the Egyptian Eastern Desert). In this case, the dimensionality curse, spectral mixing, and lineaments extraction are reasonably tackled. As the textural characteristics are a function of the spatial resolution of the input data and the applied kernel size, our study tested three kernel sizes (3 × 3, 7 × 7, and 11 × 11) over two main pixel sizes (2.5 m and 10 m) to determine which provided the best output.

2. Geological setting

The study area is located in the Egyptian Eastern Desert (Fig. 1a), which constitutes the northern part of the Nubian shield, and the western part of the Arabian Nubian Shield (ANS). The study area is well-known for its higher gold potentiality (Shebl and Csámer, 2021b; Zoheir et al., 2019). Due to its economic importance, several researchers have studied the geology of the study area (Helba et al., 2001; Shebl et al., 2022; Shebl and Csámer, 2021c, 2021a; Zoheir and Weihed, 2014). Geologically, the study area is covered by ophiolitic components mainly represented by serpentinites (Fig. 1b) and their related rocks, including talc-carbonates and Listwaenite (iron carbonate silica) ridges. Serpentinites form mostly conspicuous mountainous rocks and are widely distributed within the study area, however; smaller sized blocks could be found. These blocks are mainly distributed within highly tectonized volcaniclastic metasediments as a mélange matrix, which covers a considered area in the southern part of the study area (Fig. 1b). Besides these ophiolitic segments, island arc metavolcanics constitute a considered part of the study area, mainly at the southwestern corner. Based on previous studies and our field observations, these metavolcanics are mainly composed of andesite and andesitic metatuffs. Intrusive rocks are mainly represented by metagabbro-diorite and granitic rocks. The former are occasionally exemplified in the southern part of the study area and are almost foliated, while the latter is represented by a post-orogenic pluton (Gabal Mueilha). These rocks are dissected by dykes with different compositions and trends.

3. Materials and methods

3.1. Datasets

Sentinel 2 and the Panchromatic Remote-sensing Instrument for Stereo Mapping (PRISM) datasets were implemented in this research. Sentinel 2 optical data provides high-level land surface monitoring with about 290 km swath width using the multispectral instrument (MSI). According to its band designations (Table 1), Sentinel 2′s efficiency in various geological applications was evident. Additionally, it provides a higher spatial resolution (up to 10 m) compared to the frequently utilized satellites in geological remote sensing (e.g., ASTER, Landsat 7 and 8, etc.). The Sentinel 2 satellites (A and B) were launched by the European Space Agency (ESA), and their products were accessible through the Copernicus Open Access Hub. In this study, a cloud-free S2A_MSIL1C scene (geometrically corrected top-of-atmosphere reflectance) was implemented and handled using the Sentinel Application Platform (SNAP) and QGIS.

According to our aim (textural analysis), which strongly depends on the spatial resolution of the datasets, 2.5 m pixel-size PRISM data was adopted to pansharpen Sentinel 2 data. This instrument (PRISM) was mounted on the Advanced Land Observing Satellite (ALOS). PRISM data was geometrically corrected to zone 36 north UTM projection using the WGS-84 datum in SNAP.

Table 1
Characteristics of sentinel-2 data.

Band	Spectral region	Central wavelength (μm)	Spatial resolution (m)
1	Ultra blue	0.443	60
2	Blue	0.490	10
3	Green	0.560	10
4	Red	0.665	10
5	VNIR	0.704	20
6	VNIR	0.740	20
7	VNIR	0.782	20
8	VNIR	0.842	10
8a	VNIR narrow	0.865	20
9	SWIR water vapor	0.945	60
10	SWIR cirrus	1.375	60
11	SWIR	1.610	20
12	SWIR	2.190	20

VNIR = visible near infrared, SWIR = short wave infrared, and TIR = thermal infrared.

3.2. Methods

Several band combinations were built to better discriminate and visualize the rock units within the study area. A 10 m false color combination (12–6-2 in RGB) introduces one of the best results for the lithological content differentiation within the study area. This composite was then pan-sharpened using PRISM data to get a higher level of texture-related details with a 2.5 m pixel size. Toward a simplified paradigm for better lithological and structural mapping, only a single band was selected to compute textural attributes within the study area. After several trials, the best results were reported using band 12 as an input. This may be attributed to the superiority of SWIR bands in discriminating different functional groups of common minerals, hence their frequent usage in most geological applications. So, at this stage, two different spatial resolutions (10 m and 2.5 m) of band 12 are prepared for further detailed textural analysis.

GLCM (Grey Level Co-occurrence Matrix) or grey-level spatial dependence matrix (Haralick, 1979; Li et al., 2011) was adopted in our research to perform a comprehensive textural analysis due to its efficiency reported over different kinds of datasets, e.g., aeromagnetic (Eldosouky and Elkhateeb, 2018) and radar (Ghosh et al., 2022) datasets for lithological mapping. Basically, textural attributes could be detected by measuring spatial variability among neighboring pixels. Thus, a moving kernel (window) with a size that depends mainly on the desired output is implemented to decipher the textural characteristics by checking the digital values or numbers of all the image pixels. Additionally, this kernel allows for better analyzing the relevance among all the pixel pairs (i and j within the matrix p) with a level of detail depending on the kernel size and the spatial size of the utilized images. The kernel size is represented by the number of pixels (N); for instance, for a 7x7 window, N = 49. Through this second-order statistical analysis, several attributes including mean, variance, homogeneity, contrast, entropy, and correlation are calculated. The whole process of the adopted approach is introduced in Fig. 2.

3.2.1. Mean

It highlights the distribution of the image pixels through the moving kernel. It is considered a kind of smoothing and calculated through the following formula:

$$\text{Mean} = \sum_{i,j=0}^{N-1} iP(i,j)$$

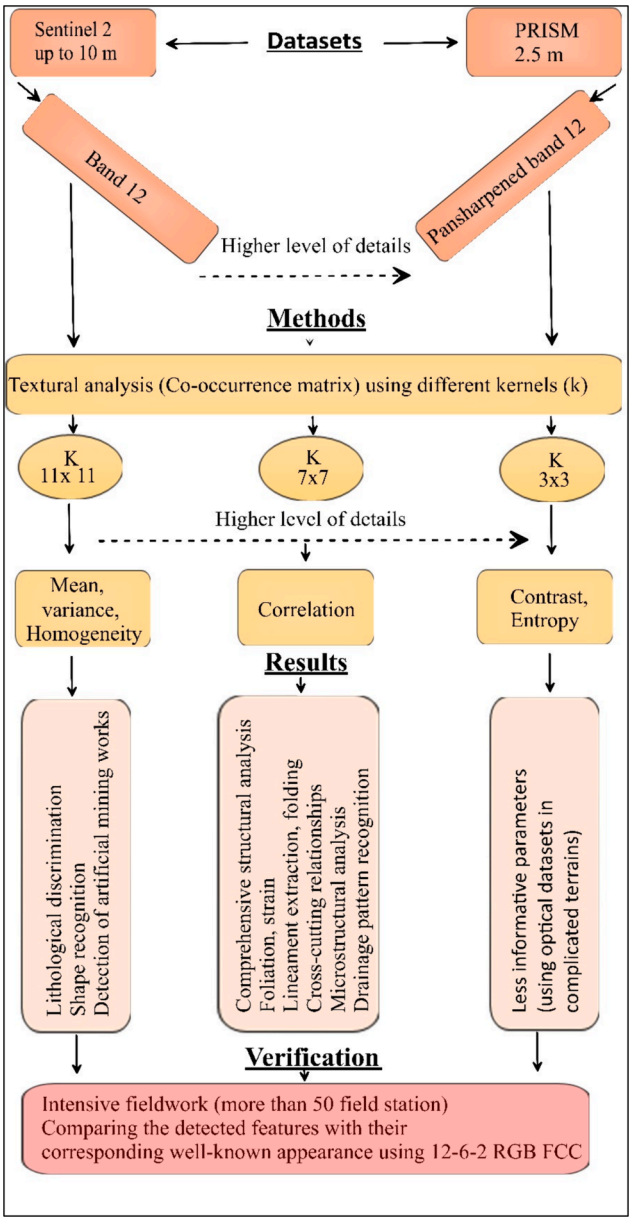

Fig. 2. Flow chart methodology adopted in the current research.

3.2.2. Variance

One of the most important parameters in textural analysis is data dispersion (Li et al., 2011; Woodcock and Harward, 2007), which could be computed through the following formula:

$$\textit{Variance} = \frac{1}{N}\sum_{i,j=0}^{N-1}(Mean - P(i,j))^2$$

The coarser the features, the higher the variance value; thus, a kind of sorting for the image constituents (different pixel values representing various rock units) could be achieved using the variance data, allowing, for instance, better lithological discrimination.

3.2.3. Homogeneity

As the name suggests, homogeneity is supposed to be at its optimum (highest) value for the same pixels (same object), and the lower values are given to higher tonal differences in a pixel pair. It could be calculated using the following formula:

$$\text{Homogeneity} = \sum_{i,j=0}^{N-1}\frac{P(i,j)}{1+|i-j|}$$

3.2.4. Contrast

It measures the internal variability among a set of image pixels. For instance, coarser textures result in higher contrast values, and zero contrast is always evident among contiguous identical pixels. Accordingly, pixels with different spectral signatures (tonal differences due to varied mineralogical compositions) could be identified by a higher contrast. It could be computed using the following formula:

$$\text{Contrast} = \sum_{i,j=0}^{N-1}(i-j)^2P(i,j)$$

3.2.5. Entropy

It measures the amount of disorder and intricacy in the image. The higher textural complexity and variability result in higher values of entropy. The latter could be calculated using the following formula:

$$\text{Entropy} = \sum_{i,j=0}^{N-1}P(i,j)\log(P(i,j))$$

3.2.6. Correlation

Correlation characterizes the linear dependencies among the adjacent pixels. Thus, higher values of correlation clearly indicate a linear relationship (mostly a structural element in our geological context) between the pixel pairs. Consequently, correlation is the main pillar for detecting several structural features, including foliation, dykes, faulting, folding, and strain measurement. This could be achieved by tracking the resultant lines, just like interpreting a seismic section. Actually, this operation facilitates extracting and interpreting various minor and major structural features with various scales and levels of details (by changing the input pixel size up to 2.5 m and the kernel size up to 3x3). Mathematically, correlation could be computed using the following formula:

$$\text{Correlation} = \sum_{i,j=0}^{N-1}\frac{(i-\mu)(j-\mu)P(i,j)}{\sigma_i\sigma_j}$$

4. Results

4.1. Lithological mapping

Our methods (mean, variance, homogeneity, contrast, entropy, and correlation) have different capabilities in discriminating all the rock units within the study area. Additionally, the extracted amount of details depends mainly on the spatial resolution of the input data (2.5 m or 10 m) and the moving window size (3 × 3, 7 × 7, or 11 × 11). Generally, our findings indicate that the best textural parameters to be utilized for a reasonable lithological mapping are mean, variance, and homogeneity. For instance, the mean layer, as a simple kind of smoothing, could give clear discrimination for serpentinites in dark brown colors (Fig. 3), granitic rocks and mining activities in bright light colors, metavolcanics and metagabbro diorites in a combination of cyan-yellow colors due to their wide variability in composition within the study area, as shown in Fig. 3. In the central part of Fig. 3, a minute distribution of serpentinite blocks (dark brown) could be easily distinguished in a matrix of different colors (cyan and yellow representing volcaniclastic metasediments) that typically indicates a kind of chaotic mixing representing the ophiolitic mélange (Kusky et al., 2020) within the study area. This central part was collectively mapped in several previous studies as an ophiolitic mélange (Shebl et al., 2022; Zoheir et al., 2019); however, in this study, only through the mean values, a higher level of details could be introduced in the specific mapping of the mélange matrix or at least separating their

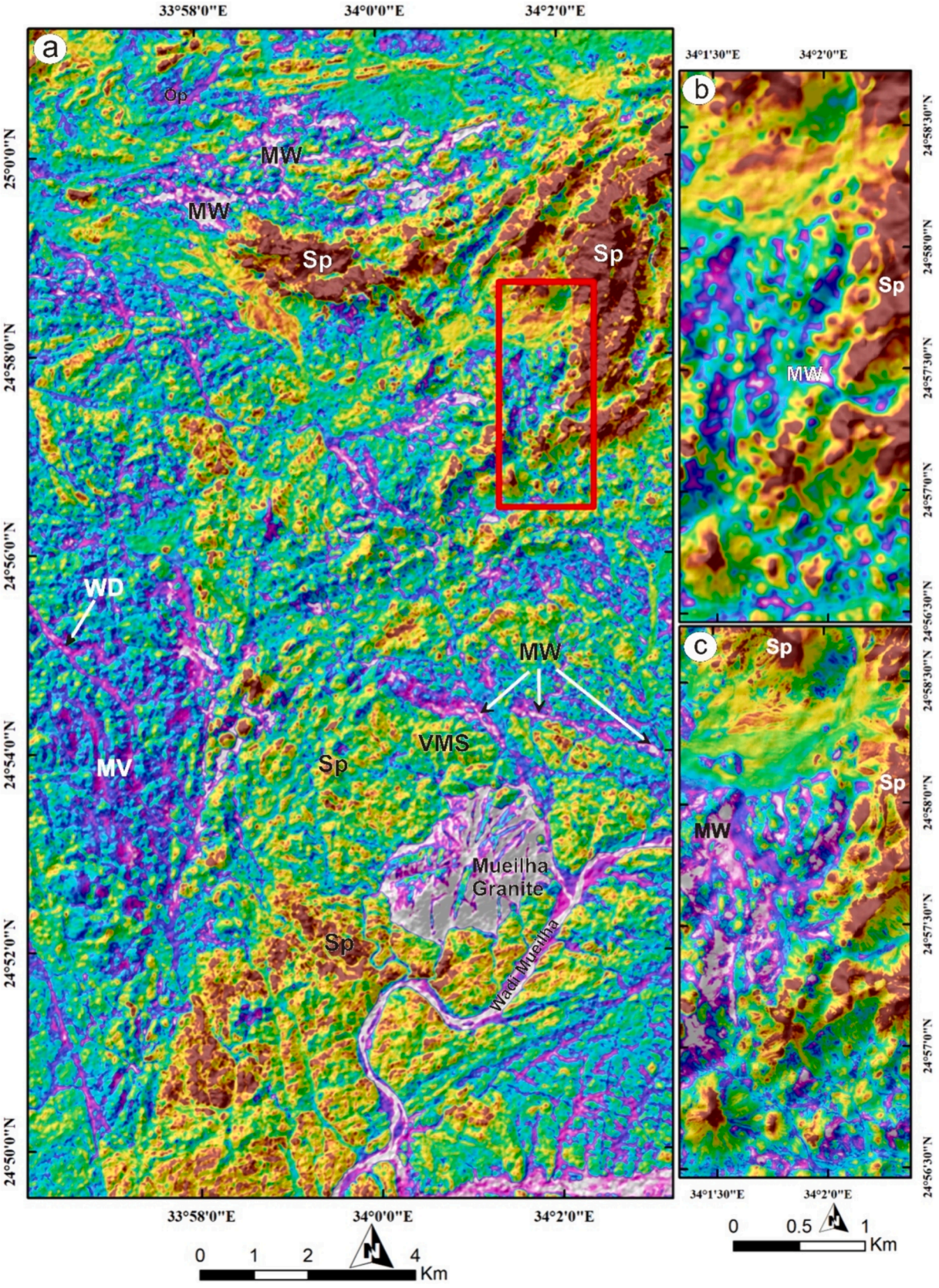

Fig. 3. (a) A pseudo-colour map representing the mean values of band 12 sentinel 2 data (10 m pixel size) created using a moving window size of 3x3 delivering reasonable lithological discrimination. The red rectangle represents a selected part from it (b) to be compared with (c) 2.5 m pixel size pan-sharpened data using the same kernel size highlighting the higher level of details with the increased pixel size. Abbreviation, Sp: Serpentinite, MV: metavolcanics, VMS: volcanic meta-sediments, MW: mining works, WD: wadi deposits.

dominant blocks, e.g., serpentinites. Additionally, a pseudocolor representation of the mean values gives insight for detailed and minute mapping, especially with small-sized kernels and higher spatial resolution data. For example, a part of the study area (the red rectangle over Fig. 3) was selected to compare the results of two inputs (10 m and 2.5 m) using the same kernel size (3 × 3). A greater amount of details could be extracted using the finer spatial resolution, as shown by the detailed delineation of artificial mining works (pinkish to whitish colors) in the western part of the subsetted images (Fig. 3 b and c). Furthermore, a definite delineation of serpentinite bodies is achieved in the image, especially when comparing, for instance, the upper part of the subsetted images (Fig. 3 b and c), where serpentinite blocks are precisely outlined and even separated from the weathering products of serpentinite itself by tonal differences.

A combination of mean, variance, and homogeneity greatly enhances the lithological discrimination within the study area, as shown in Fig. 4a and 4b. In the pseudocolor ramp of mean, variance, and homogeneity in RGB, respectively, serpentinite rocks are clearly discriminated in blue, metavolcanics in yellow, some kinds of wadi deposits and mining work zones in red, and the pinkish colors mostly represent the ophiolitic mélange matrix (consisting regularly of volcaniclastic metasediments and metagabbros). The power of kernel size and input data spatial resolution is manifested by comparing, for instance, the black rectangles over Fig. 4a and 4b. The best choice for the lithological mapping depends mostly on the purpose of the study. Generally, comprehensive lithological mappings with a 10 m output are mostly accepted; however, for comparative studies, detailed structural studies, and areas of potential economic interest (e.g., the case study), both resolutions and various kernel sizes are recommended. Commonly, both Fig. 4a and 4b delivered an acceptable lithological allocation, especially when the case study is one of the most complicated terrains (Neoproterozoic basement rocks with multi-stage structural deformation, dykes, weathering, alteration zones, mining works, etc.); however, differences could be sensed through the black boxes over the figures. We strongly expect distinguished results from this approach when implemented over less complicated terrains (i.e., sedimentary rocks).

Respective RGB representation of homogeneity, mean, and variance using a kernel size 11 × 11 delivers reasonable lithological discrimination for most of the rock units within the study area, as shown in Fig. 4c. In the latter, serpentinite blocks are represented in red, metavolcanics in yellowish green, most of the mining work areas in cyan, metagabbros, and their weathering products in orange. This combination is strongly recommended for further lithological investigations over similar terrains due to its adequacy in separating artificial mining works and some alteration zones (cyan), besides its competency in separating most of the complex related to deformed contact boundaries of rock units within the study area. Additionally and upon several trials, implementing any of the other textural parameters couldn't deliver any more advantageous (compared to homogeneity, mean, and variance in RGB, respectively) results in lithological mapping. For instance, embedding correlation output with the mean and variance in an RGB combination of correlation, mean, and variance (Fig. 4d) may give an acceptable lithological mapping, but it is barely good when compared to Fig. 4c. Consequently, our research strongly advocates implementing an RGB of homogeneity, mean, and variance, respectively, as a standard composite for detailed lithological mapping in future studies.

4.2. Comprehensive structural analysis

One of the most important findings in our research is resolving the complicated structural setting through the identification of several elements, including foliations, folding, faulting, cross-cutting relationships, etc. This issue is rarely tackled by previous studies dealing with textural analysis; however, it greatly delivers better analysis for structurally complicated terrains with a degree that could be as precise as fieldwork. Occasionally, this approach could deliver a more adequate identification (not only by highlighting the structural elements but also its hosting rock context, so it could greatly help in fathoming the regional structural framework) than traditional field studies, especially when a high resolution 2.5 m pixel size input is adopted. Our findings indicated that the most important data in analyzing the structural framework is the correlation pattern, as it measures the linear dependencies in the input data (Li et al., 2011). The identification level (i.e., major or minor structures) that might assist in resolving complex structural patterns over various observational scales is strongly controlled by input pixel and window size variances.

Foliation delineation, as one of our novel results, could be completed through an RGB combination of correlation, mean, and variance using a kernel size of 7 × 7 for the southern part of the study area (Fig. 5a). This combination is substantially recommended for further structural examinations, whatever the purpose of the study, as it could give a comprehensive context about the main structural trends, detailed minor structural relationships with color changes based on the hosting foliated rocks and the dominant wadi trends that could help in further interpretations. For instance, two major trends of foliation (divided by a NE-SW fault-controlled wadi) are clearly identified in Fig. 5a, the first of which is in the upper part and clearly shows a NE-SW orientation. These lines not only specify the foliation trends, but also the line color itself (black or green) and its background give information about the hosting rocks and the associated structural features, i.e., green lines typically depict the structurally controlled wadis. Black lines with pinkish backgrounds characterize the mélange matrix and basic metavolcanics. Black and green lines represent highly dissected rocks of metagabbros and acidic metavolcanics. Tracing every single line could give a huge amount of information about the rock unit distribution and their structural relationship, just like interpreting a seismic section. For instance, several minor displacements (faults) are conspicuous in the northwestern part (just beneath the wadi bend) of Fig. 5a, and Fig. 5b was provided for better comparison. Additionally, the response of the rock units (having the same trend) to the same force (deformation event) could be sensed by interpreting the upper part into other minor sections but with different colors and line densities. This is confirmed by the high strain representation (strong shearing) in the southern part of the upper foliation trend (ENE-WSW) compared to the northern part of the image. Detailed inspection for the first foliation trend (Fig. 5a) could result in minute structural details that could be useful in resolving the structural history of the study area.

The second major structural trend displayed in Fig. 6 represents the southern part of the study area (clearly manifested just by comparing the upper and lower parts of Fig. 5a). A perfect identification of a parallel (NNE-SSW trending at the southeastern part of the study area) and trellis drainage patterns (direct indicators for structural control) could easily be achieved by looking at the green lines representing the wadis (Fig. 5a). The study facilitates the identification of the dominant drainage patterns just by gathering single-colored (green) lines. The orientation of gabbroic rocks (NW-SE) is clearly seen in a pictorial form. Further inspection reveals a perfect identification of basic and felsic dykes in different forms. Mafic dykes are represented by dark blackish lines within a pinkish background; felsic dykes are shown as light green lines on a lightish brownish background (Fig. 5a). A focused analysis of these dykes revealed that they could be easily identified by their trends and cross-cutting relationship by visualizing the mean values, as shown in Fig. 6a and 6b.

Additionally, and over a scale of meters, our investigation gives insights about minor deformations or host rock minute structures associated with a certain event (which can be observed, for example, by finding perpendicular lines within the dashed circles over Fig. 7a), which may cause geologists to reconsider the potential significance of that point or this region. For example, Fig. 7 shows a clear demarcation for a dextral displacement related to a certain deformational event affecting the southern part of the study area. This dextral sense of displacement could be easily depicted by tracing the shifted dikes

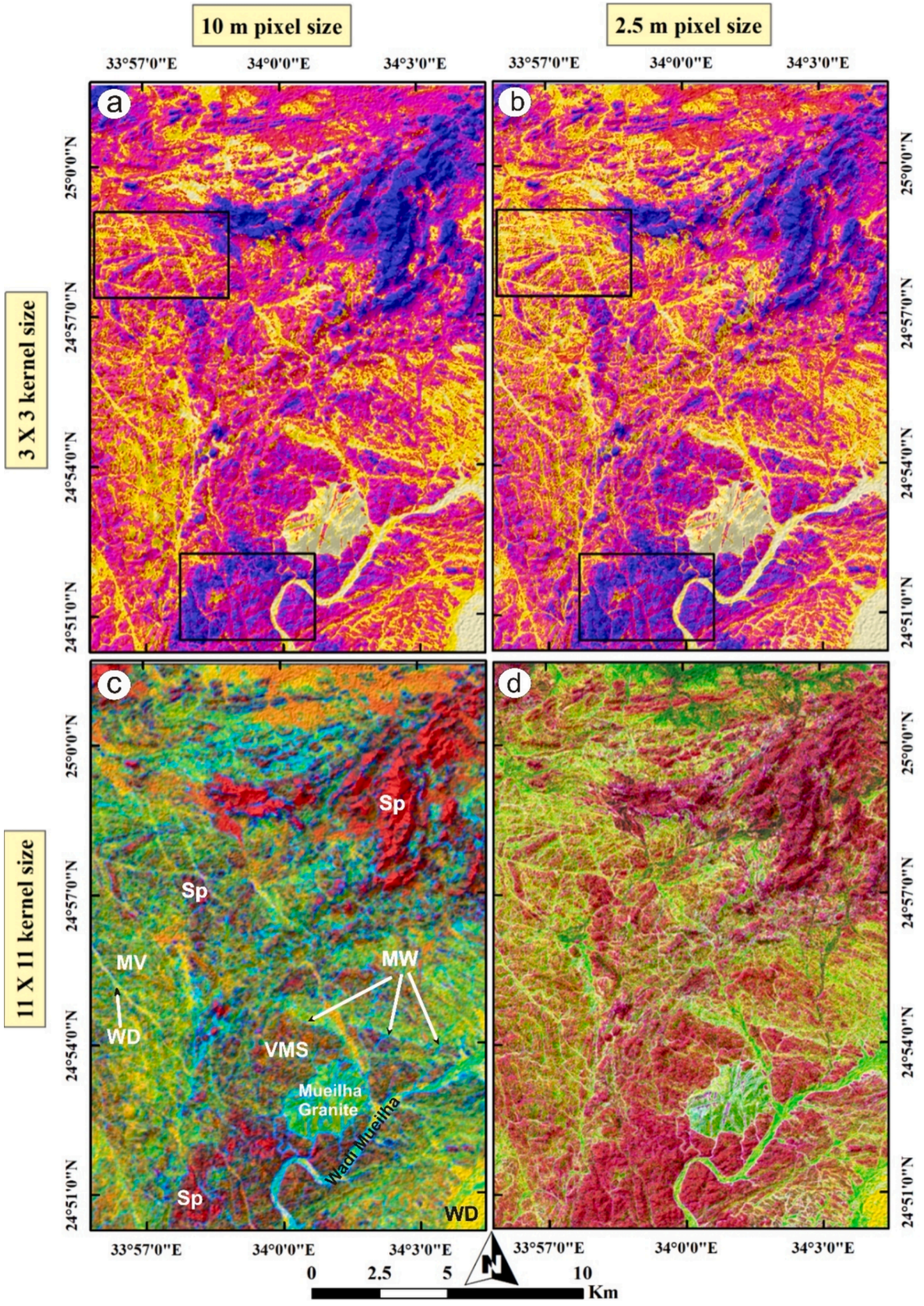

Fig. 4. Illustrates the cell size effect of the input image and the moving kernel for the co-occurrence matrix outputs by displaying the pseudocolour ramp of Mean, Variance, and Homogeneity combination resulting from (a) 10 m and (b) 2.5 m pixel-size inputs with the same kernel size (3x3). Black rectangles for comparing the amount the extracted details. Lithological discrimination using respective RGB composites of (c) Homogeneity, Mean, and Variance, and (d) Correlation, Mean, and Variance. Abbreviation, Sp: Serpentinite, MV: metavolcanics, VMS: volcanic metasediments, MW: mining works, WD: wadi deposits.

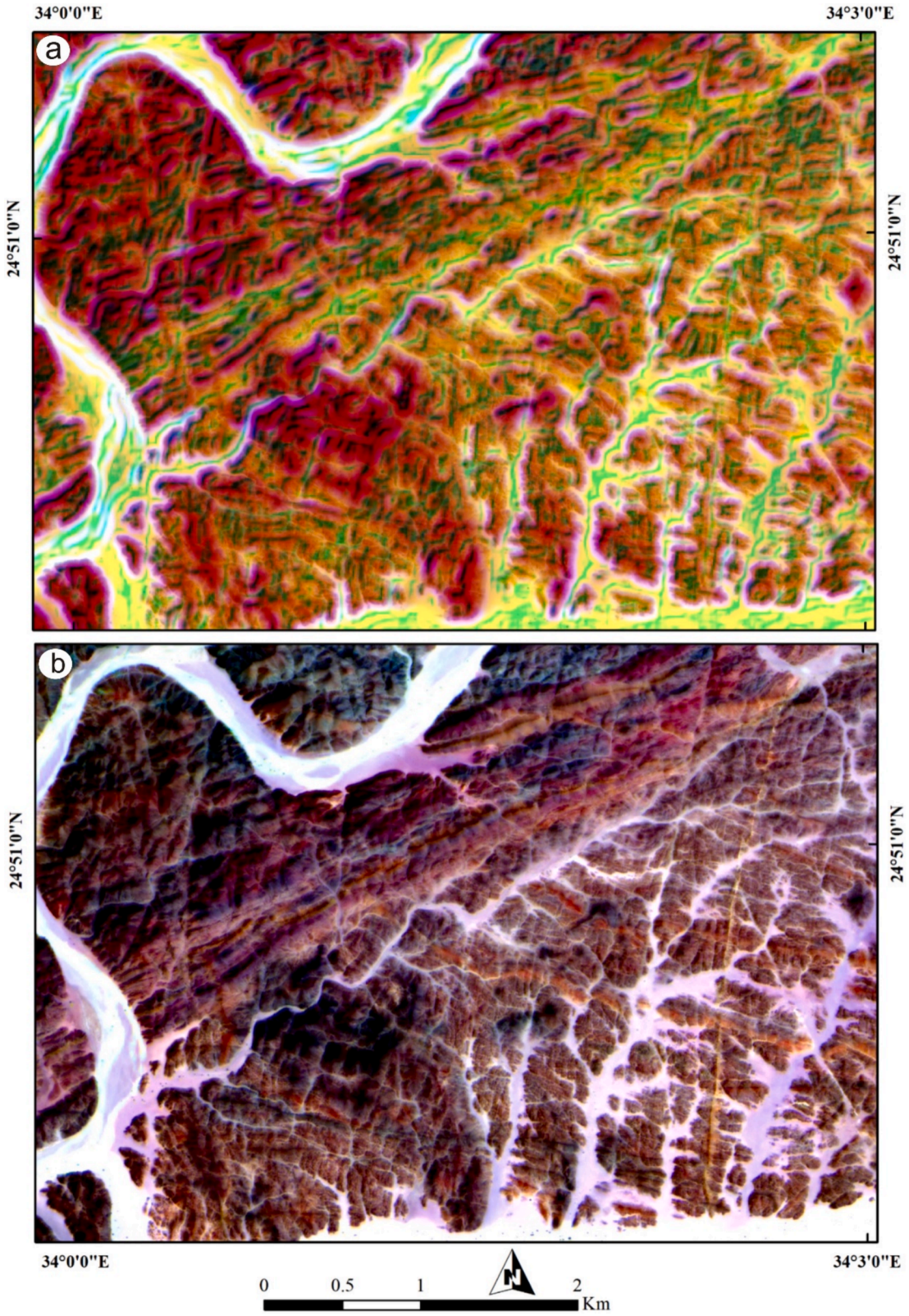

Fig. 5. (a) ENE alternative purple and green streaks delineating foliation patterns using an RGB of correlation, mean, and variance, respectively. (b) RGB of bands 12–6-2 for comparison and verification.

(Fig. 7b). The adopted approach (Fig. 7a) offers a fair extraction for the same sense of motion within the country rocks (dashed shapes over Fig. 7a) on both sides of the clearly-displaced dike, despite the fact that typical visual remote sensing representations (Fig. 7b) cannot perceive these minute displacements within the country rocks at this scale. This is one of the major advantages of our study, as it is sometimes very difficult to detect small-scale structural features from the normal visual interpretation, and not all the structures can be covered and studied through

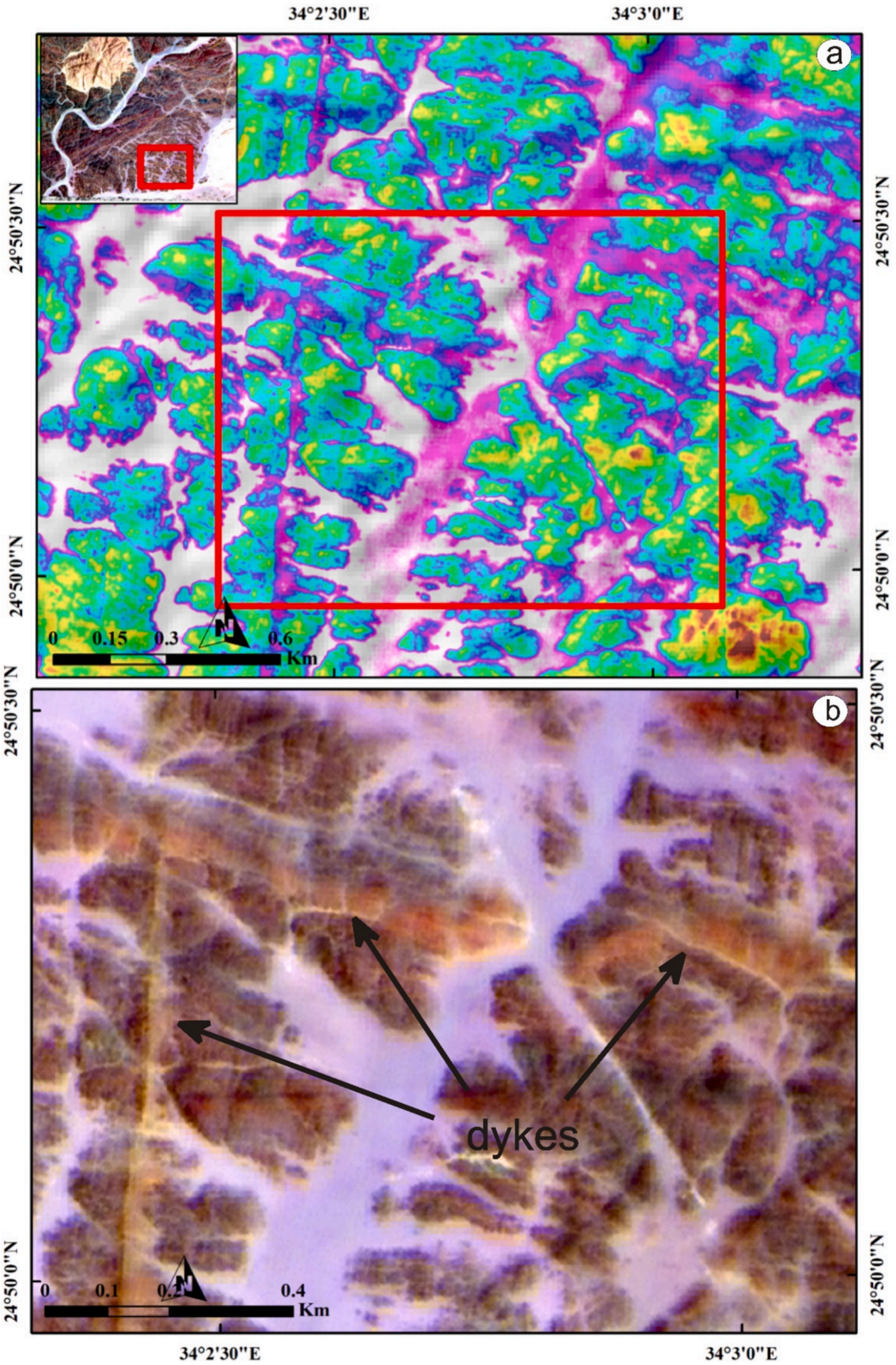

Fig. 6. Perspicuous detection of conjugate dykes that show a cross-cutting relationship using (a) mean values visualization. (b) RGB of bands 12–6-2 for comparison and verification.

traditional fieldwork.

Based on the above, using this kind of textural-based structural analysis, the locations of various structural relationships could be delineated according to the purpose and scale of further studies, allowing better final geological interpretations that could help in, for example, detecting structurally controlled mineral deposits. Consequently, this investigation provides a simplified tool for detecting several spectacular structural features, including

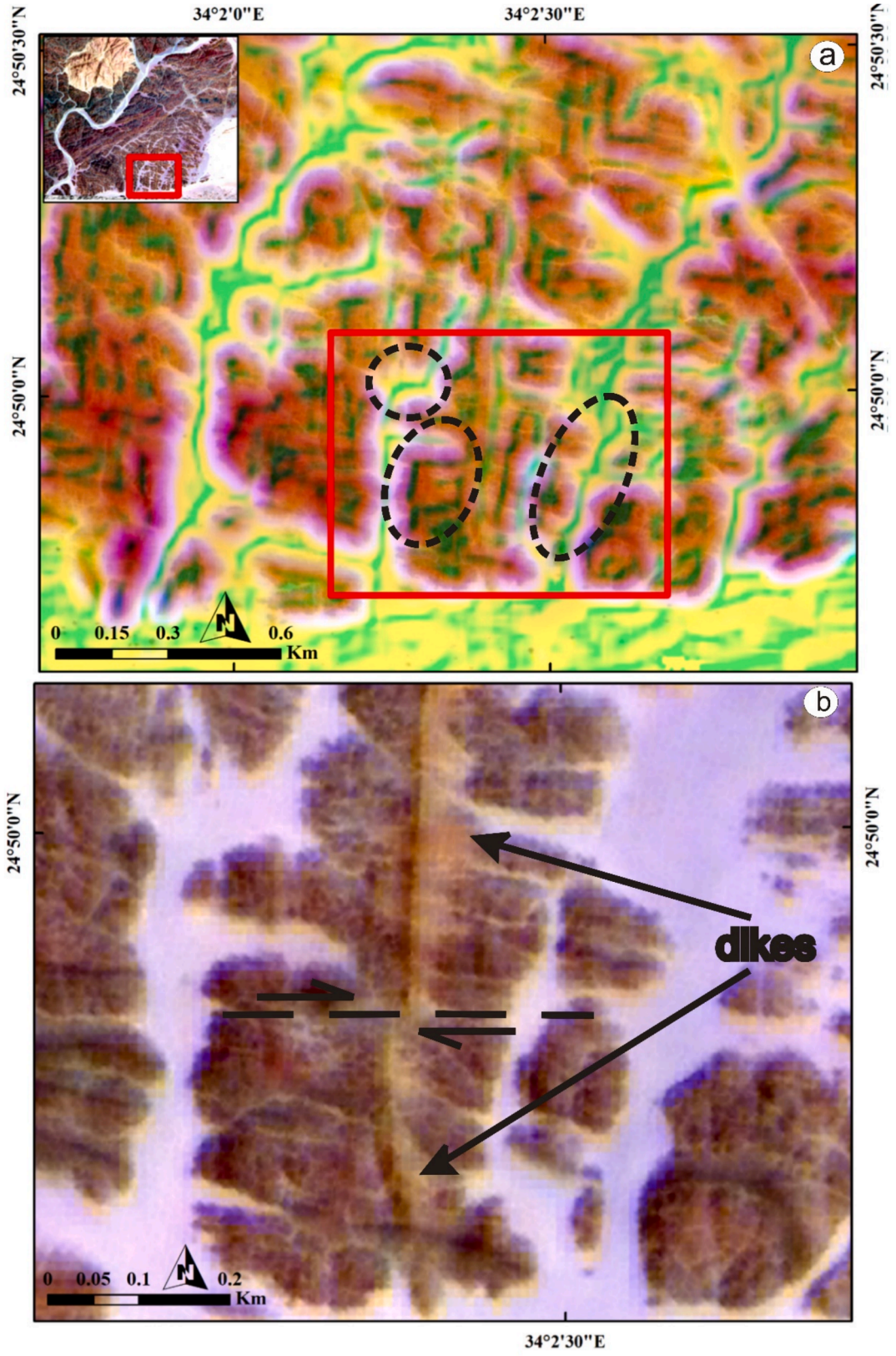

Fig. 7. (a) RGB of correlation, mean, and variance respectively, manifesting minor structural relationships within the host rocks (through the green lines showing late-stage dextral lateral displacement marked by dashed black circles) that could be obliterated or missed during visual interpretation or fieldwork (b) RGB of bands 12–6-2 for comparison and verification.

1. drainage patterns indicating structural control (parallel and trellis as shown in Fig. 5),
2. dikes composition (Fig. 5) and their cross-cutting relationships (Fig. 6), with their reverberations within the surrounding rock units (Fig. 7a),
3. foliations (Figs. 5 and 8) with their orientations and an indication for the response of the foliated rocks to a deformational event,
4. fold-like structures (Fig. 9a and 9b), and.
5. different types of displacements (representing faults) exist within various rock types (Fig. 9c and 9d).

4.3. Lineament extraction

Automatic lineament extraction has become one of the fundamental issues in several research fields, including remote sensing, geological, hydrogeological, engineering, and landslide susceptibility analyses. Consequently, one of the main targets of the recent research is to measure the efficiency with which textural analysis results in the perfect delineation of various linear features. Our results indicate a surpassing description of lineaments, not only by highlighting the linear features as lines but also sometimes indicating the width and depth of these lineaments (especially wadi-controlled lineaments). For instance, the Mueilha granitic pluton is well-dissected by multiple structural lineaments in various directions (Fig. 10). A combination of correlation, mean, and variance of a 10 m input image using an 11x11 kernel size in RGB gives a superb depiction of all the linear features (Fig. 10a). The comparison of Fig. 10a with the real linear features (Fig. 10b) clearly indicates how well this combination performs in detecting all linear features (major and minor) in different color representations depending on the characteristics of the detected lineament. For instance, a structurally controlled wadi (wide lineament zone) is distinguished as an area with whitish pink borders and central blue lines with varying color intensities according to the steepness and depths of that zone (Fig. 10a). Other smaller linear features are represented by green lines distributed over a yellow background that represent the texture of the granitic body. A lucid cross-cutting relationship is well-expressed with varied colors intensities indicating various characteristics of those intercepted lines, as shown at the southwestern part of the granitic body where an NNW-SSE trending whitish lineament (wide and deeper) crosscut a green NE-SW trending lineament (narrow).

A more detailed extraction of minor lineaments could be achieved by using a kernel size of 3x3 over the same input pixel size (10 m). For example, these wider zones are closely investigated to extract their lineaments, and the cross-cutting NNW-SSE is divided into two parts, the lower part with a pinkish hue (deeper) and the upper green part (shallow), as shown in Fig. 11. Furthermore, several minute lineaments are extracted in green lines distributed over the yellowish background (granitic body representation); all of these green lines are compared with the real image (2.5 m), and the excellent coincidence is obvious. This kind of lineaments (scale of meters) may open the door for microstructural studies using textural analysis over remote sensing data, which could save a lot of time and effort in further investigations. This was supported when displaying the resultant linear features using a 2.5 m input image (Fig. 12).

Besides the efficiency of textural parameters' combinations in lithological mapping and comprehensive structural analysis, it greatly helps to identify regular and irregular shapes of different bodies with a reasonable degree of discrimination and a higher degree of differentiating the original rock texture from the weathering products. For instance, two volcanic cones are precisely distinguished in Fig. 13a by different colors, i.e., the deep brown color indicates the richness in mafic content within the original rock mass, and the yellowish and greenish together represent various lithological compositions (i.e., weathering products or metavolcanic representations) as shown in Fig. 13a and b. Additionally, the same Fig. 13 indicated how well the artificial mining sites are depicted (in whitish pink) even the placer mining along the wadi deposits that has been confirmed at the suggested locations in the field. Similarly, Fig. 14 clearly shows a perfect identification of an irregular metavolcanic rock body, with different colors exactly representing its varied composition. Moreover, some random mining sites around that rock body also were detected (pinkish-white zones). These random artificial mining sites could be highly specified or obliterated depending on the utilized input spatial resolution and the adopted kernel (Fig. 15). The latter also clearly indicates the pixel-size effect in the appearance of an NW-SE narrow wadi that was obliterated in 10 m pixel size input data compared to that of 2.5 m pixel size.

Our results have been checked and verified through field investigations and petrographic examinations. We conducted a field exploration trip to the study area, aiming to define and verify the exposed lithologies and some of the detected structural features at the meso- and micro-scales. The locations of the selected field photos are given in Fig. 16 to help understand the observed field features with our results within the geological context of the study area. Our field investigations confirmed the eligibility of the adopted approach in lithological mapping and revealed that the study area is dominantly occupied by Neoproterozoic Pan-African nappe assemblages and post-orogenic granites as it well-known for the central Egyptian Eastern Desert (Badawi et al., 2021). The most prevalent rock assemblage is the Pan-African nappe assemblage, which consists of metavolcanics and island arc associations (Fig. 17 a), ophiolitic mélange, metagabbro, and volcaniclastic metasediments (Fig. 17 b). These rock units and their placer deposits have been heavily explored for ores (mainly gold) for several decades (Fig. 17 a and c). In the background of Fig. 17 c, a cone-rock body could be seen that is previously displayed in Fig. 13 using our approach, in addition to the locations of active mining works manifested in both Fig. 17c and 13 a.

The ophiolitic sequence within the study area is composed mainly of serpentinites and metagabbros, whereas the island arc association is made up of schists (Fig. 17 d), metasediments, and metavolcanics. After that, post-orogenic activity was represented by the Mueilha granite intrusion (Fig. 17e) in the southern part of the study area. This intrusion related prolonged activity was responsible for several pegmatitic dikes that were recorded in the surrounding rocks nearby Gabal Mueilha. Both (the pegmatitic dikes and their host rocks) have recently shifted along two conjugate brittle fault sets with dextral and sinistral shear directions (Fig. 17 f and g). Coinciding with our results in lineaments extraction, Mueilha post-orogenic granite is highly dissected by several joint sets (Fig. 18 a). Additionally, several structural elements, e.g., S-C' fabric (Fig. 18 b) and quartz veins along fractures were detected at various locations. These structures were found proximal to highlymineralized and already mined (Fig. 18 c) zones (detected in our approach) and more or less related to the ophiolitic serpentinite (Fig. 18 d), which is considered a potential source for mineralization enrichment in the study area. This relationship confirms the role of structural elements as a pathway for hydrothermal fluids' migration, especially in orogenic gold deposits, which is the case in our study area.

Besides visual verification and field investigations, a petrographic examination was carried out in our research to introduce rigorous evidence for some of the detected features over a microscopic scale of observation. For instance, and as a predominant rock unit within the study area, the metavolcanics are hard, fine-grained, and dark grey to green in color. They are predominantly andesitic and made of plagioclase, biotite, quartz, hornblende, and chlorite. The accessory minerals are iron oxides and epidote. Plagioclase phenocrysts are embedded in fine-grained plagioclase, biotite, and chlorite groundmasses. Epidote, sericite, and iron oxides represent the alteration products. Coinciding with our results and field observations, petrographical investigations revealed that these *meta*-andesites are severely deformed during the brittle phase, as indicated by the sinistral displacement of plagioclase phenocrysts that have undergone complete alteration to sericite (Fig. 19a).

The post-orogenic granites are exposed as a high mountainous peak

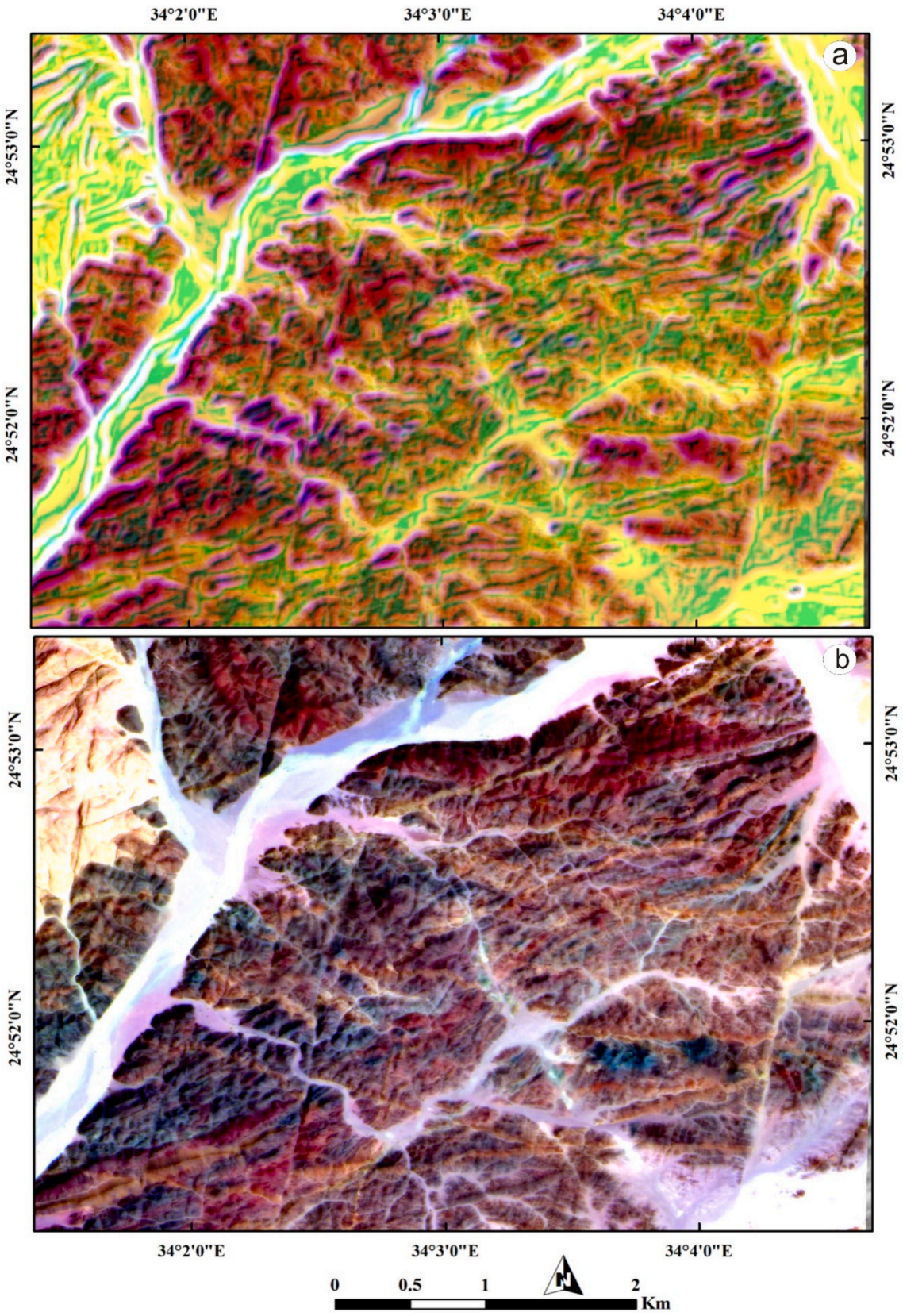

Fig. 8. (a) Lineaments elicitation and foliation delineation using an RGB of correlation, mean, and variance respectively. (b) RGB of bands 12–6-2 for comparison and verification.

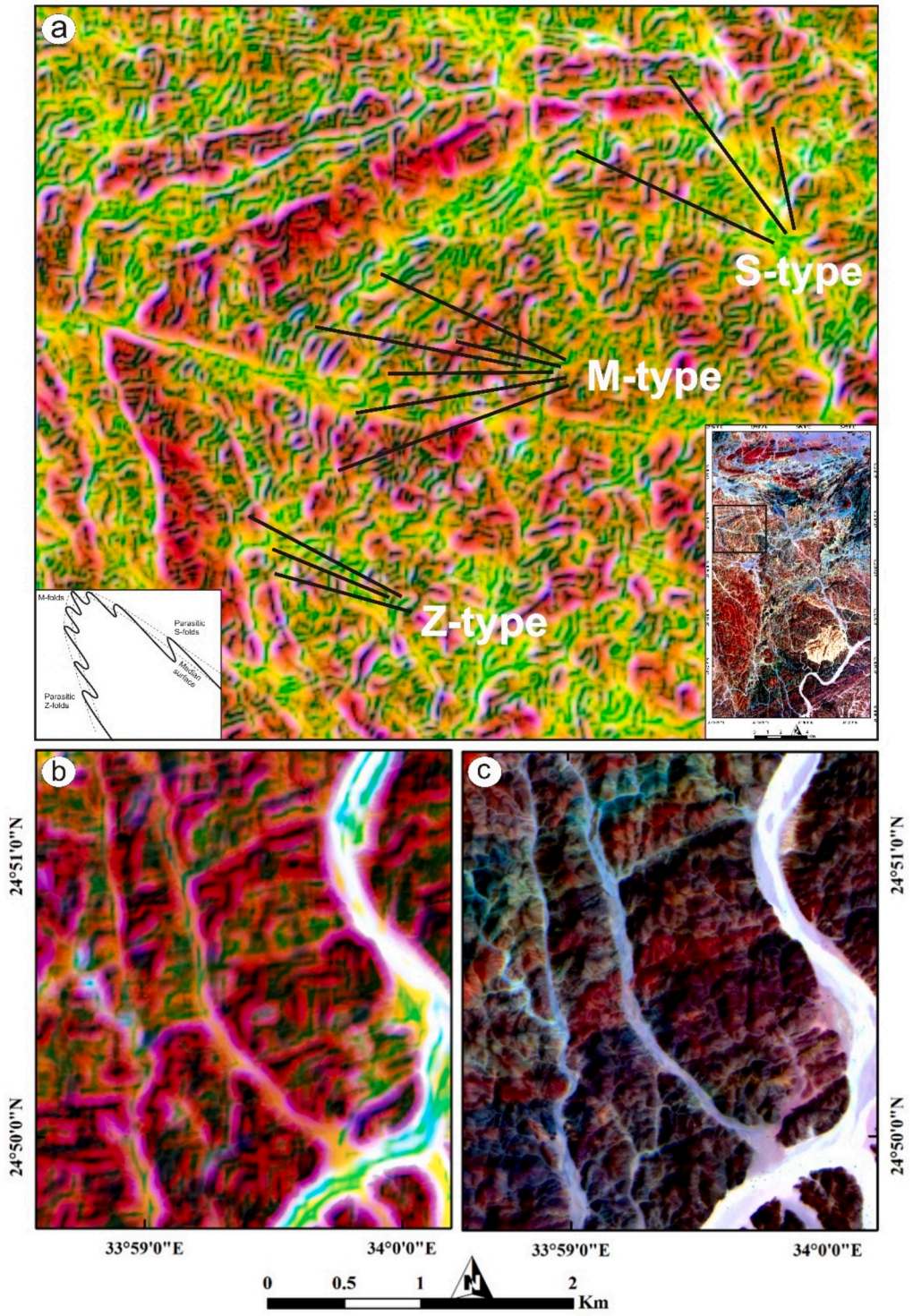

Fig. 9. Obvious delineation of structural elements including (a) Antiform structure showing s, z, and m patterns and (b) fault-related displacements using an RGB of correlation, mean, and variance, respectively, and (c) RGBs of bands 12–6-2 for clarification and verification.

of the Mueilha magmatic pluton, forming an ellipsoidal shape with the long axe trending roughly in the NE-SW direction (Fig. 10). This pluton is distinguished by its strong contacts intruding the surrounding pan-African nappe (Fig. 17 e). This pink, coarse-to-medium-grained granitic pluton ranges in composition from syenogranites to monzogranites (Fig. 19c). Their composition consists primarily of quartz, biotite, plagioclase, orthoclase, and microline. The alteration phases consist of kaolinite, epidote, sericite, and iron oxides. The reorientation of quartz and feldspar porpyroclasts, which form an imbrication array and sigmoidal rotated pebbles, is indicative of a late stage of sinistral displacement at a shallow crustal level. In addition, these granites have N-S en echelon extension gashes and veins, which we assume formed along the NNE-SSW sinistral shear zone (Fig. 19 b, d, e). We believe that some of the deformational features identified at the brittle phase in Mueilha granites and surrounding metavolcanics are consistent with those observed using the textural analysis technique, e.g., the large-scale brittle fault in the NNE-SSW direction with sinistral shear sense of motion in the studied area.

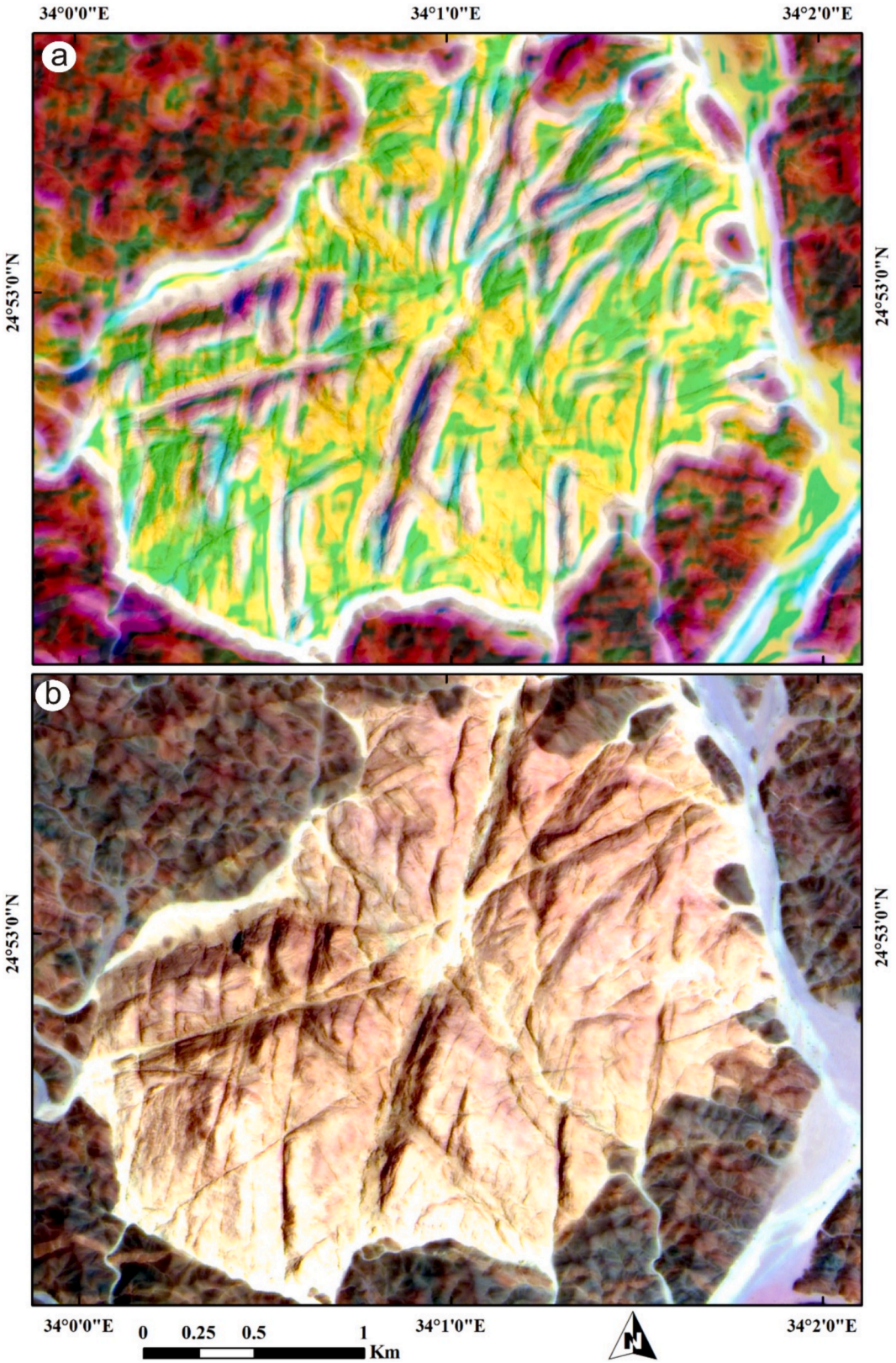

Fig. 10. (a) Generalized representation of Mueilha granite lineaments using a combination of correlation, mean, and variance (created by a 10 m input image and an 11x11 kernel size) in RGB, respectively. (b) RGB of bands 12–6-2 for clarification and verification.

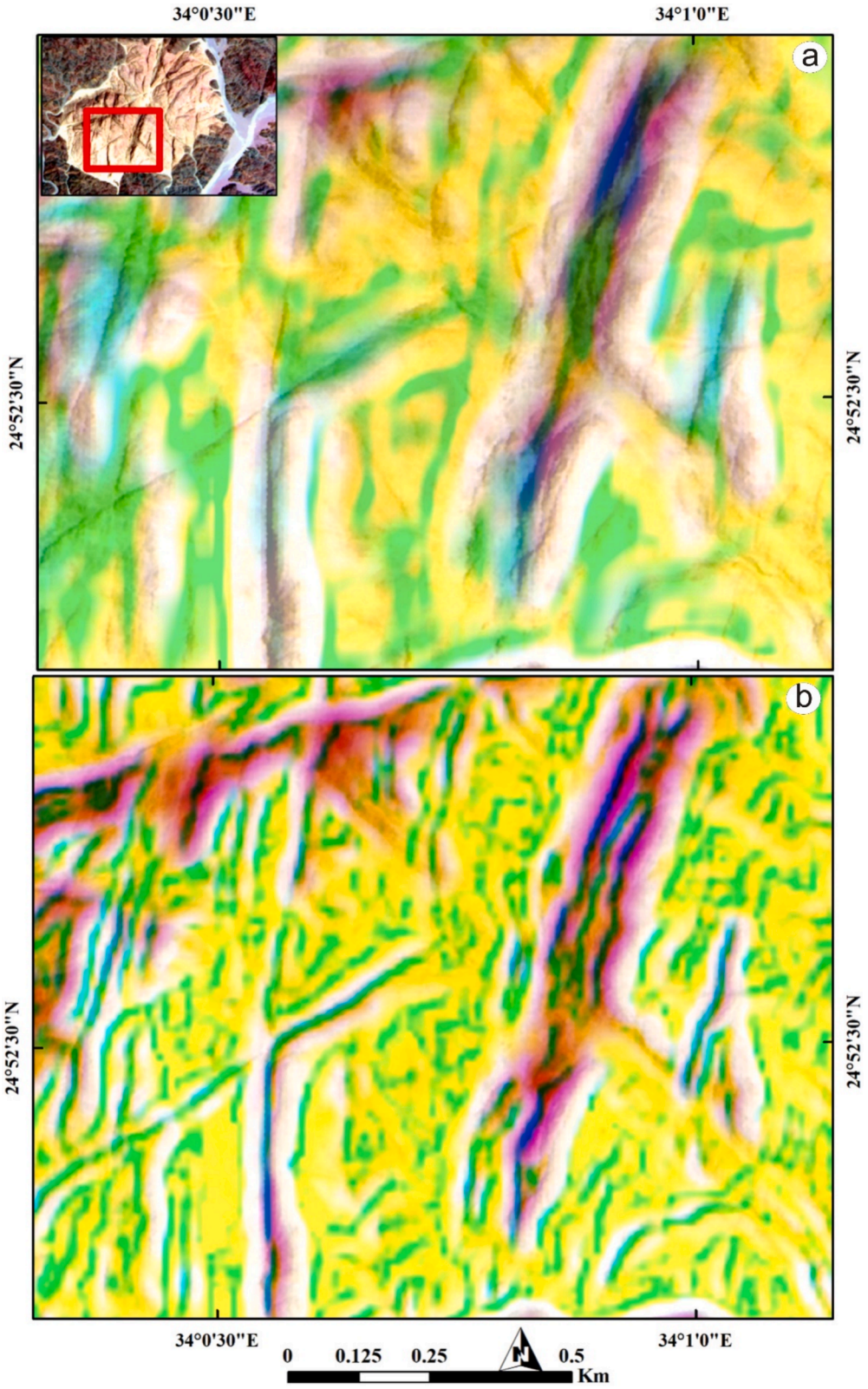

Fig. 11. Detailed inspection for some of Mueilha granite lineaments using 10 m input pixel size data by applying (a) 11x11 and (b) 3x3 kernel sizes to show the lineaments characteristics (e.g., depth, steepness, minor linear features) using a combination of correlation, mean, and variance.

5. Discussion

Our research introduces a simplified approach to avoid the dimensionality curse mostly associated with remote sensing data (to save the time of handling several bands for lithological and structural analyses). This was conducted by applying textural analysis using different kernel sizes (3×3, 7×7, 11×11) over single Sentinel 2 band data (2.5 m and 10 m) to get the textural attributes, including mean, variance,

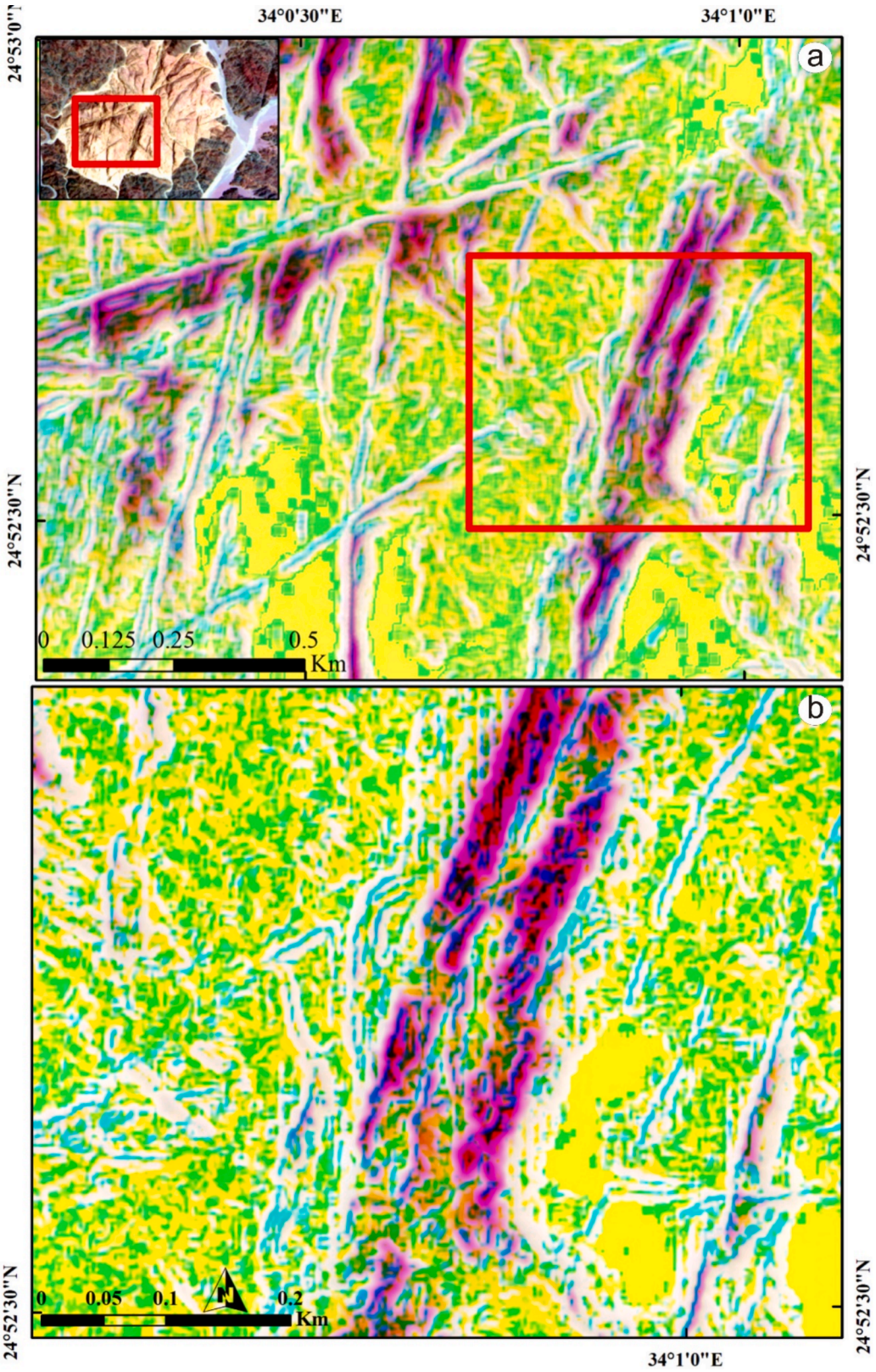

Fig. 12. Thoroughgoing examination for a part of Mueilha granite lineaments using a 2.5 m input pixel size data by applying (a) 3x3 kernel sizes. The extracted amount of details may obscure the original granitic texture (yellow color). (b) This level of detail (scale of observation) could help in further detailed microstructural studies of remotely sensed indicators.

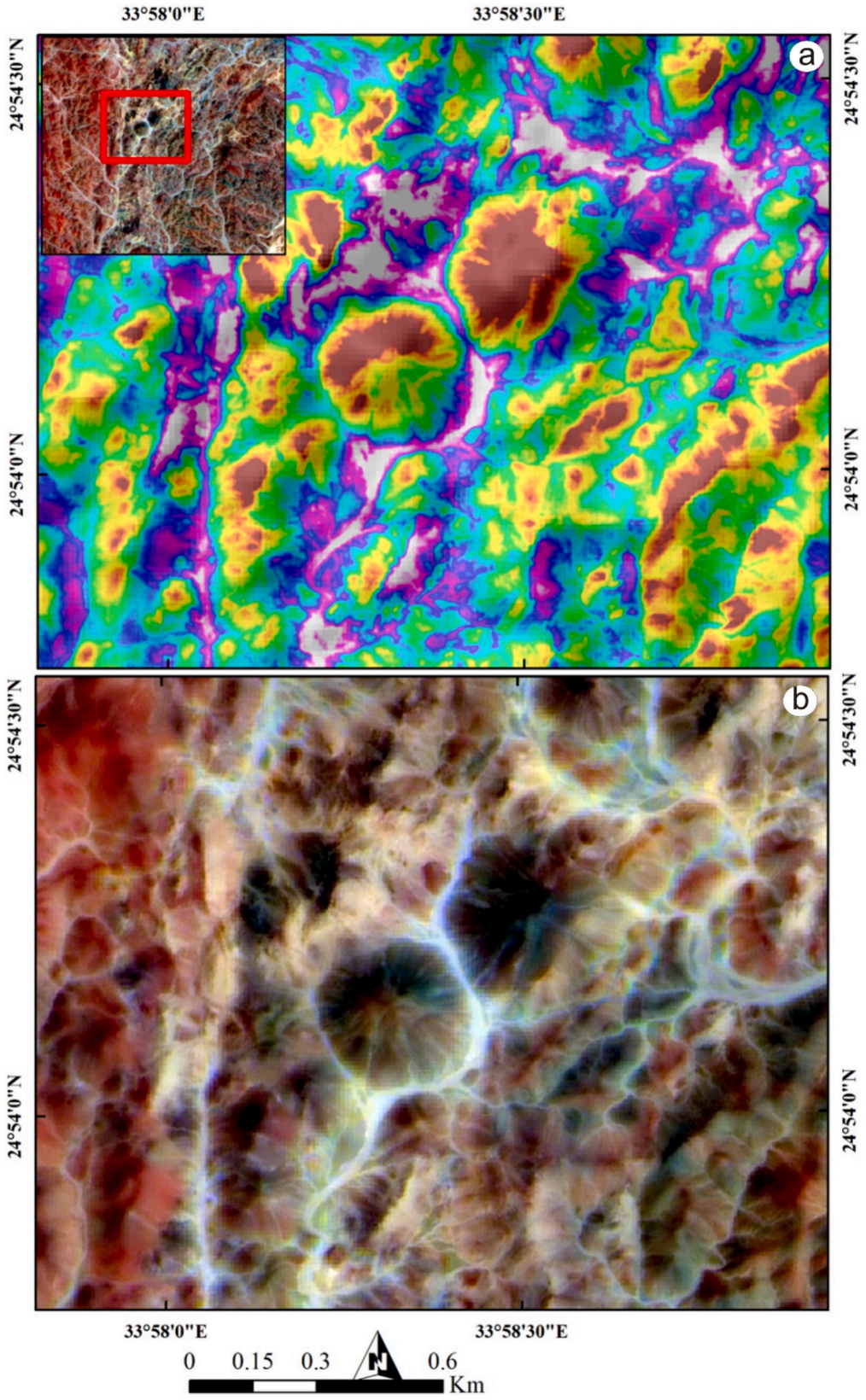

Fig. 13. (a) Recognition of two cones with compositional discriminations using (a) mean values visualization. (b) RGB of bands 12–6-2 for comparison and verification.

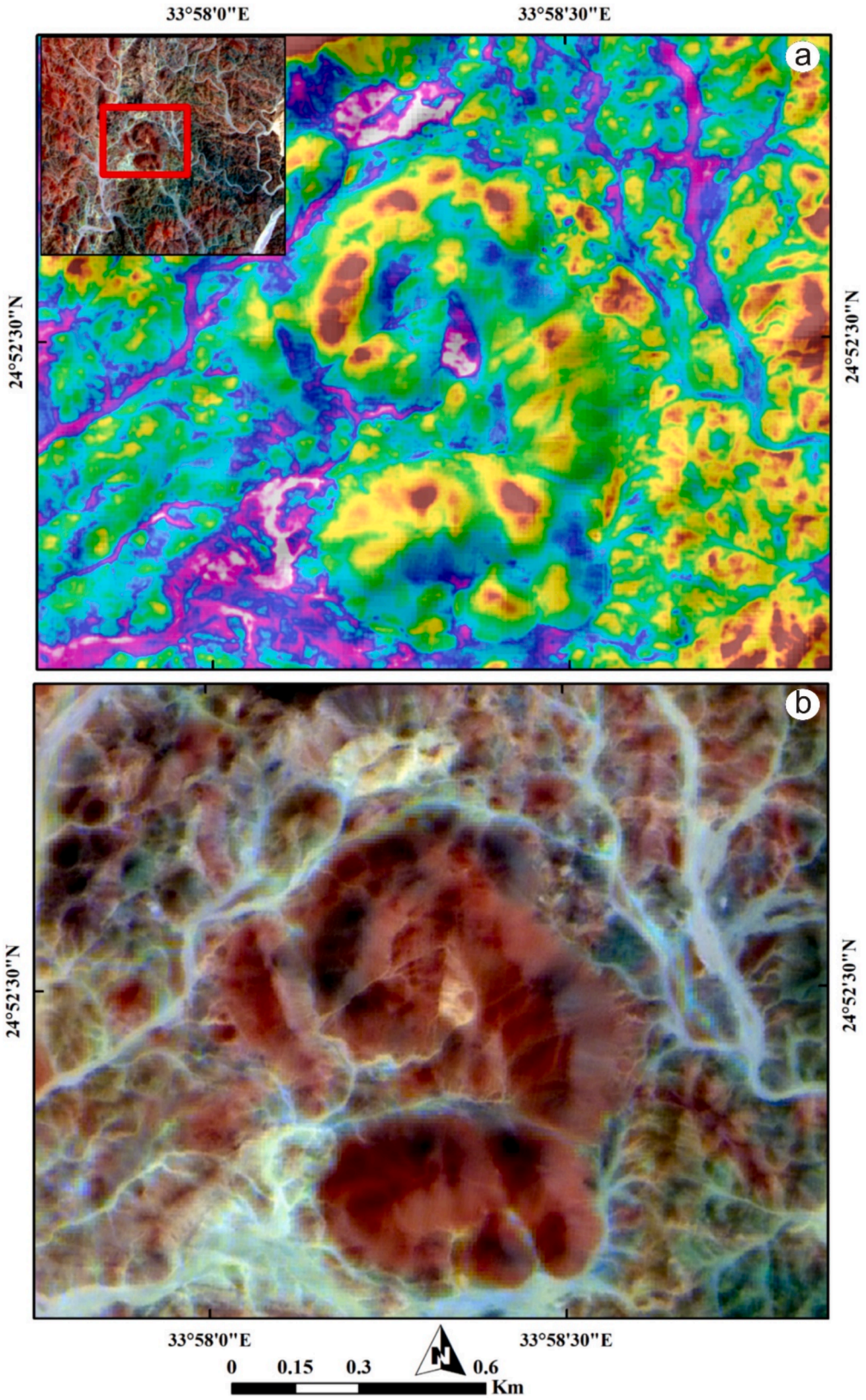

Fig. 14. (a) Delineation of irregular and heterogeneous volcanic bodies with an adequate specification of their different parts. (b) RGB of bands 12–6-2 for clarification and verification.

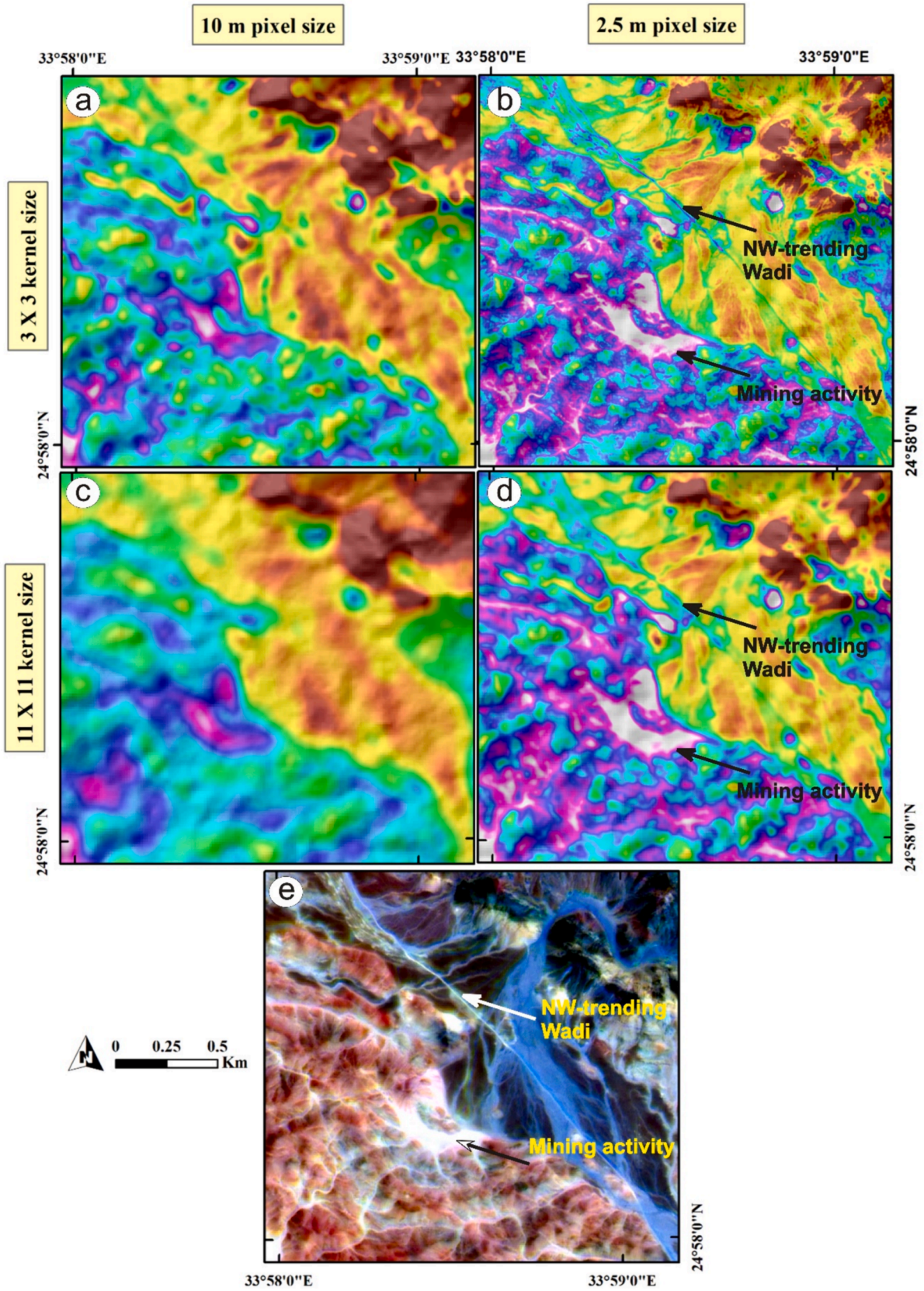

Fig. 15. Pixel and kernel size effect in the specification (of mining activities in pinkish white) or obliteration (of NW-SE diagonal trending wadi) for different features using kernel sizes of (a, and b) 3x3 and (c, and d) 11x11. (e) RGB of bands 12–6-2 for clarification and verification.

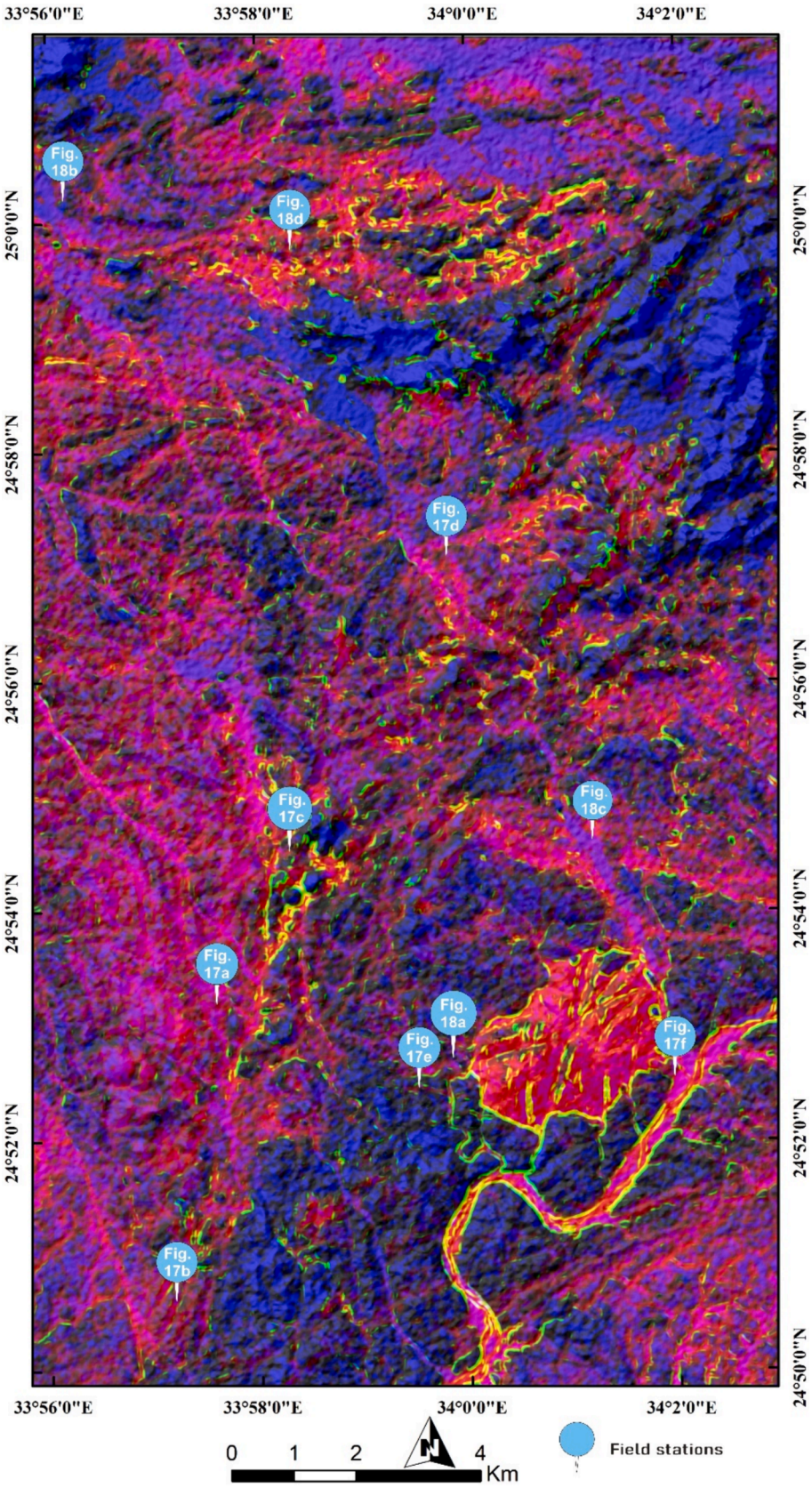

Fig. 16. A Pseudo-colour map showing the distribution of field stations that is displayed in Figs. 17 and 18.

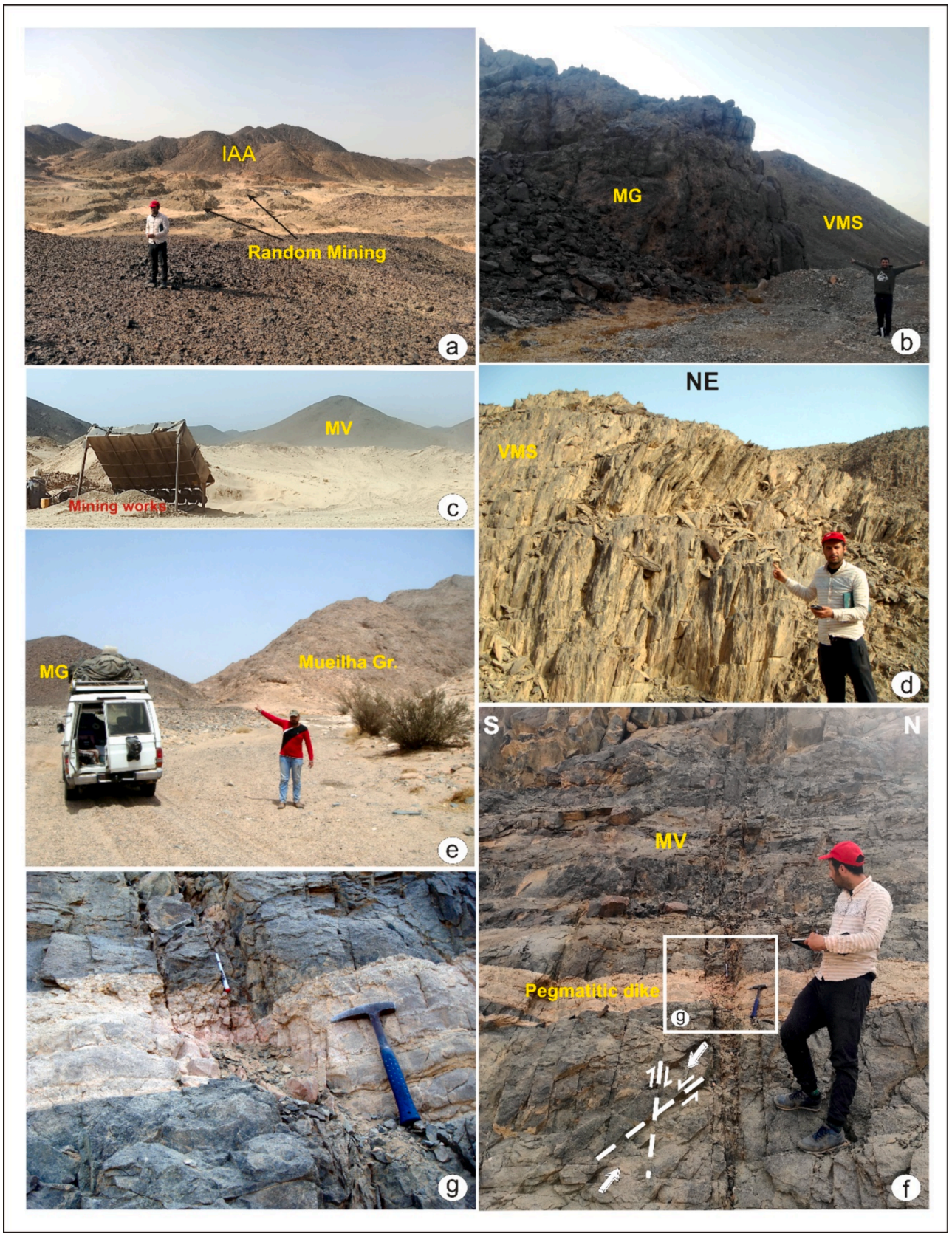

Fig. 17. Field photos of the study area showing (a) exposures of island arc assemblage (IAA), (b) ophiolitic metagabbros (MG) and volcanic metasediments (VMS), (c) active mining for placer deposits, (d) nearly vertical VMS, (e) intrusive contact of Mueilha granite with gabbroic rocks, (f & g) conjugate faults sets intersecting metavolcanics (MV) and pegmatitic dikes.

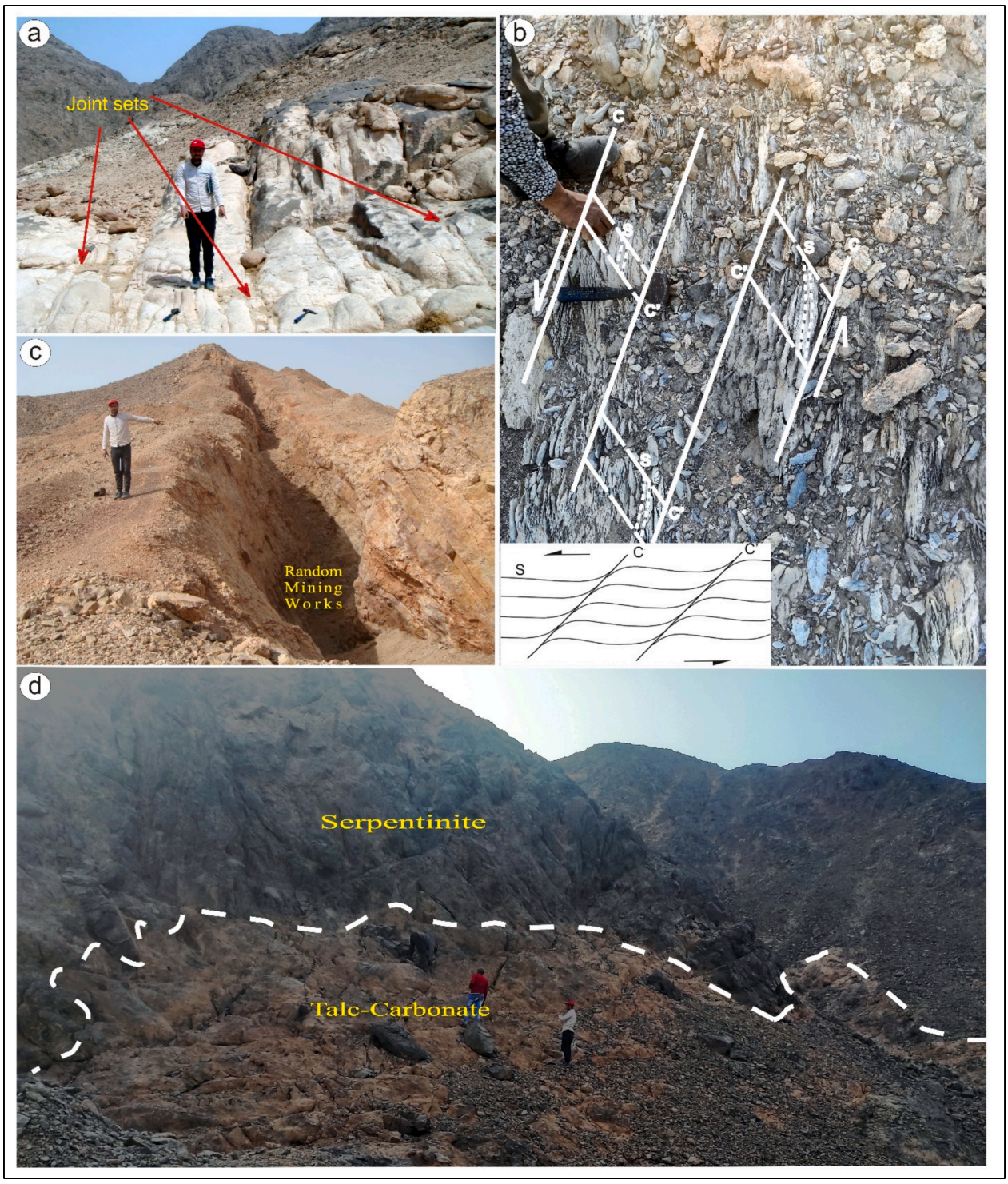

Fig. 18. Field observation of the study area showing (a) exposures of Mueilha granite dissected with systematic joint sets, (b) mining activities, (c) S-C' fabric of volcanic metasediments (VMS) with sinistral shear sense, and (d) serpentinites and their associated talc-carbonates.

homogeneity, contrast, entropy, and correlation. Through some suggested combinations of these textural patterns, various information could be obtained, facilitating geological interpretations for further investigations. Our approach's findings exceed the frequent remote sensing analysis in lithological and structural mapping by highlighting several attributes within the study area that are difficult to find in normal RGB remote sensing interpretations and over a metric scale that is impossible to cover in traditional field observations.

Compared to interpreting optical (multispectral or hyperspectral) combination results, textural interpretations are a bit complicated (Dentith, 1995) but substantial for comprehensive geological analysis. As it analyzes the data from a different aspect (not only the spectral signatures) related to tonal intensities and spatial relevance of the image pixels (Haralick, 1979). Thus, a considerable amount of information (mostly related to the inherited or deep structure of the image pixels) is supposed to be released with textural analysis compared to optical data processing alone. This could be explained by the binary pixel attributes in the textural analysis where each pixel has local variability and spatial

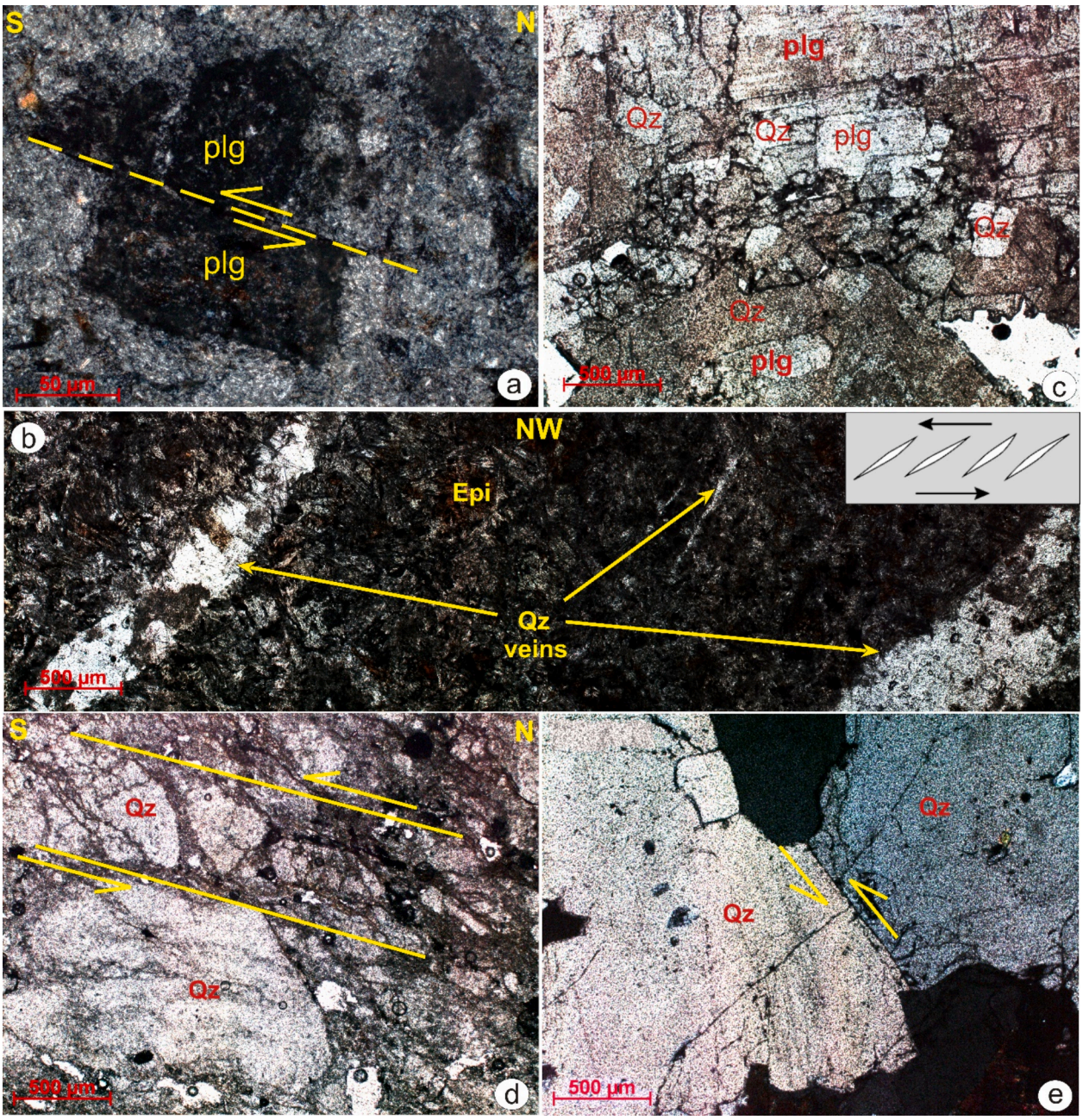

Fig. 19. Thin-section photomicrographs showing (a) porphyritic texture of *meta*-andesites showing heavily altered plagioclase phenocryst with sinistral dislocation (xN); (b) en echelon quartz veins (xN), (c) heavily fractured coarse-grained granites of Mueilha pluton (ppl), (d) sigmoidal train of quartz porphyroclasts along sinistral shear zone (ppl), (e) late stage left-lateral strike slip fault dislocating heavily fractured quartz grains relatively (xN). Abbreviations, Qz: quartz, Pl: plagioclase, Epi: epidote.

regularity (Li et al., 2011). For instance, each cell possesses its own local variability simultaneously within its regional regularity context (with the surrounding pixels). According to these local and regional variabilities, several geological examinations could be achieved. Using the same spatial attribute and for the first time, our research applied statistical-based textural analysis over 2 different pixel sizes (2.5 m and 10 m) for the study area to get a higher level of details and a closer view of the local and regional variabilities of the image cells. Additionally, spatial variability is enhanced by implementing three different kernel sizes (3 × 3, 7 × 7, and 11 × 11), which could greatly help in analyzing local and regional structural features besides providing reasonable discrimination for the rock units. Our results indicated that a larger amount of details could sometimes overfit the target (detailed geological examinations) by implementing a 3 × 3 window size image over a cell size of 2.5 m. However, it could open the door for microstructural analysis using remote sensing data that may be required for detailed exploration programs.

The other main goal of this study is to help the geological community solve the dimensionality problem (larger data sets and more time and work because there are so many bands) and the data availability problem. Textural analysis could be a great solution which deliver a significant quantity of geological details using a single band (all the textural parameters derived using band 12 only). For example, it could tackle of foliations, lineaments, cross-cutting relationships, reverberations of a certain structure over the country rocks, rock drainage patterns, shape recognition of systematic rock bodies, quaternary deposits delineation, etc. Sentinel 2 Band 12 was selected in this investigation due to its higher level of geological discrimination in the grey scale images

compared to the other bands, besides the efficiency of SWIR bands in geological applications (Shebl et al., 2022, 2021). Sentinel 2 and PRISM data were picked out in our research due to their higher spatial resolution compared to the common optical datasets (Shebl and Csámer, 2021a). This (spatial resolution) is a crucial concern to deliver reliable, detailed geological explanations using textural analysis. This was for instance demonstrated by getting unsatisfactory lithological mapping results when implementing textural analysis over coarse spatial resolution Landsat TM data (Li et al., 2011). Regarding the data availability issue, our study selected multispectral data as it is the most commonly utilized remote sensing data in various applications. Textural analysis in various studies incorporated different data types such as gravity (Cooper, 2004), aeromagnetic (Eldosouky and Elkhateeb, 2018), TerraSAR-X (Mahmoud et al., 2011; Pradhan et al., 2014), and airborne polarimetric TopSAR (Radford et al., 2018). However, these data sources, unlike multispectral datasets, are not easily accessible to the entire geological community. Others implemented optical datasets, but with lower spatial resolutions compared to Sentinel 2 and PRISM data or in other applications, i.e., Land Use–Land Cover mapping (Shih et al., 2021; Tassi and Vizzari, 2020), crop residue estimating (Najafi et al., 2018), and change detection (Shakya et al., 2019). However, we could not find a detailed textural study dealing with the discrimination of the complicated surface lithological terrain and its detailed structural features using 2.5 m and 10 m spatial resolution input data. Thus, we expect our study to pave the way for future detailed geological studies through our adopted simplified approach. It is worth mentioning that the best outputs may be different when applying the textural analysis to other datasets, for instance, Eldosouky and Elkhateeb, (2018) observed that second moment, variance, and entropy are more operative than contrast, homogeneity, and correlation in delineating structural features from aeromagnetic data..

To verify our results, an optical RGB combination of sentinel 2 bands 12–6-2 was utilized to compare the highlighted features resulting from textural analysis with their corresponding well-known appearance in the false color combination. It should also be emphasized that the adopted approach clearly depicts the reverberations of a certain structural event (e.g., sense of motion of a dislocated dike) within the country rocks, which are impossible to notice using normal remote sensing RGB representations of the study area. Additionally, an intensive fieldwork and petrographical examination were performed to verify our results through 50 field stations to highlight the detected lithological boundaries, artificial mining works, alteration zones, placer deposits, and lineaments. Our field observations show a great coincidence with our textural interpretations (Fig. 16) over different scales of observations.

Besides visual interpretation, field verifications, and petrographical examinations, our findings were compared to the previous studies performed over the study area. For instance, our textural-based structural analysis of the study area reveals detailed structural elements that are in harmony with those derived from extensive field work conducted by Zoheir et al. (2019), who proposed four deformational phases (D1, D2, D3, and D4). Our analysis was able to define several deformational features that can be attributed to these deformational phases. Among these, the foliation in the south Mueilha area indicates their ENE–WSW striking is related to the D1-NNW-SSE shortening (Figs. 5, 8, and 19 d). The Beizah-Mueilha area is occupied by many macro-scale folds (Fig. 9a) that were documented as D2-NNE-SSW shortening-related structures. Additionally, the textural analysis reveals parasitic Z, M, and S folding patterns on both limbs of the master fold, whose fold hinge trends in the WNW-ESE direction (Fig. 9a). These patterns, particularly those related to the upright folds, appear much more spectacular in satellite images than other types of folds documented in the study area and coincide with what was stated by Badawi et al. (2022), who defined such multilayered minor folding patterns related to the subvertical Fatira metavolcanics from remote sensing images. Here, in the study area, our approach can perfectly clarify similar geologic features, especially those of vertical attitude, where their profiles are well preserved on map view, even better than normal RGB remote sensing images. The D1-related foliations observe zigzag folding patterns that are developed later due to D3-E-W oblique convergence (Fig. 9a). Additionally, the method of textural analysis used in this area shows that D1-related foliations, Mueilha granite, and post-tectonic dikes were displaced by the NNE-SSW sinistral fault set (Figs. 5, 6, 8, and 9). These findings, which were either confirmed by field observations conducted by us or other authors (Zoheir et al., 2019) or suggested by the textural analysis technique, demonstrate how the integration of field data and textual analysis can provide a more objective and complete perception for large-scale studies. Such studies, which necessitate detailed field exploration, will almost certainly encounter accessibility issues at outcrops due to rugged topography. From another perspective, detailed fieldwork nowadays requires a significant amount of time and money to cover such large areas of kilometers in detail, particularly for geologists interested in regional tectonic models and the structural framework. Integration with remote sensing data, which is becoming increasingly important in these situations, becomes a requirement. However, the issues regarding the quality of the visual and spatial resolution of satellite images still hamper the certainty and precision of this type of data. Consequently, textural analysis can be utilized to overcome that and provide detailed findings. Such analysis can be used in conjunction with field data to study inaccessible structures in details, as well as to complete the geologic framework on a broader scale.

As a common limitation in automated methods for geological applications, and to fully utilize our approach, we strongly recommend investigating the detected features. This verification enables a deeper understanding of their origins and provides insights into the regional context of these structural elements. For example, while our current approach efficiently extracts various structural elements (e.g., linear features) for the user, reliable investigations are necessary to check for any missed features and to distinguish between different types, such as tectonic, morphological, and anthropogenic lineaments. It should be also emphasized that one of the main strengths of our study is detailed structural mapping. However, general lithological characteristics can be depicted adequately for single-band analysis. Nonetheless, enhanced lithological interpretation could be achieved by analyzing more bands, which is part of our future research.

6. Conclusion

Upon multi-aspect verification (visually, through fieldwork, petrographic study and previous research) of our findings, we strongly recommend our approach for further detailed geological investigations. This research concludes the following:

- Using a single band (band 12 of Sentinel 2 data), almost all the required geological interpretations could be achieved with a high degree of accuracy using textural analysis. Lithological discrimination, comprehensive structural analysis (including foliation characterization, detecting dykes, faults, folds, cross-cutting relationships, and a lot of minor structures that could be extracted), drainage pattern delineation, and shape recognition are articulately accomplished.
- The current research reveals that the best methods for lithological discrimination are mean, variance, and homogeneity. This could be explained by the definition of these terms; for instance, homogeneity gives simple discrimination for similar rock units, whereas variance tries to discriminate different rock units, and the mean delivers a kind of smoothing for the original pixel values. Thus, this research strongly recommends applying those three outputs (in different ways, i.e., pseudocolor ramps or RGB combinations) in further lithological discrimination when a multispectral band is an input for this statistical analysis.
- Our study recommends adopting correlation in comprehensive structural analysis (edge detection, lineaments extraction, etc.)

compared to entropy, and the second moment, which did not give effective results in lithological or structural mapping using the adopted datasets.

- Exhaustive lineament extraction could be achieved not only by detecting the linear features, but also by obtaining vital information about their width, depth (in the case of a lineament-controlled wadi), and steepness.
- Adequate shape recognition (enhancing the lithological variability for the same body) for regular and irregular rock bodies is achieved to an accurate degree that could separate the rock body from the desert varnish, talus, or other lithological compositions.
- Original Sentinel 2 (10 m pixel size) data and the pan-sharpened PRISM data (2.5 m) delivered convenient results, but a detailed and accurate representation is achieved using both the finer spatial resolution and narrow kernel sizes.
- Adopting 2.5 m pixel input images with 3 × 3 kernels gives a large amount of information that could greatly assist in constructing a primitive microstructural pattern for a study area. This rigorous investigation could help with competent delineation of mineral deposits and alteration zones, especially the structurally controlled ones besides resolving the complicated structural frameworks from minute observations to regional or general investigations using the varied kernel and pixel sizes. For instance, 10 m input data with a kernel size 11 × 11 gives the major structural trends within the study area; however, a detailed investigation and minor tectonic events could be deciphered using a 2.5 m image size and 3 × 3 moving window size through the textural analysis. This in turn could reopen the door for new structural interpretations over different terrains by easily analyzing the major and minor deformational events related features.
- One of the most important findings in this research is that the approach can not only depict the conspicuous structural features but also highlight their reverberations within the host rocks, in a way exceeding normal remote sensing representations.
- This study proves notable results over highly complicated terrains; thus, we expect very good outputs beyond the limits of the study area and in a less-complicated geological setting (e.g., sedimentary terrains).

Funding

The current research did not receive external funding.

CRediT authorship contribution statement

Ali Shebl: Conceptualization, Methodology, Software, Visualization, Writing – original draft. **Mohamed Badawi:** Formal analysis, Methodology, Writing – original draft. **Maher Dawoud:** Formal analysis, Methodology, Validation, Writing – review & editing. **Mohamed Abd El-Wahed:** Formal analysis, Validation, Writing – review & editing. **Hanna A. El-Dokouny:** Investigation, Validation, Investigation. **Árpád Csámer:** Investigation, Methodology, Supervision, Validation, Investigation.

Declaration of competing interest

The authors declare that they have no known competing financial interests or personal relationships that could have appeared to influence the work reported in this paper.

Data availability

Data will be made available on request.

Acknowledgments

Our gratitude is extended to ESA and JAXA for generously providing the data. Ali Shebl and Mohamed Badawi acknowledge the support from the Stipendium Hungaricum scholarship, a joint executive program between Hungary and Egypt. Our heartfelt thanks go to the anonymous reviewers and the editors for their invaluable efforts throughout the review process.

References

Abd El-Wahed, M., Kamh, S., Ashmawy, M., Shebl, A., 2019. Transpressive Structures in the Ghadir Shear Belt, Eastern Desert, Egypt: Evidence for Partitioning of Oblique Convergence in the Arabian-Nubian Shield during Gondwana Agglutination. Acta Geol. Sin. - English Ed. 93, 1614–1646. https://doi.org/10.1111/1755-6724.13882.

Abdelkader, M.A., Watanabe, Y., Shebl, A., El-Dokouny, H.A., Dawoud, M., Csámer, Á., 2022. Effective delineation of rare metal-bearing granites from remote sensing data using machine learning methods: A case study from the Umm Naggat Area, Central Eastern Desert. Egypt. Ore Geol. Rev. 150, 105184 https://doi.org/10.1016/J.OREGEOREV.2022.105184.

Ahmadirouhani, R., Karimpour, M.H., Rahimi, B., Malekzadeh-Shafaroudi, A., Pour, A. B., Pradhan, B., 2018. Integration of SPOT-5 and ASTER satellite data for structural tracing and hydrothermal alteration mineral mapping: implications for Cu–Au prospecting. Int. J. Image Data Fusion 9, 237–262. https://doi.org/10.1080/19479832.2018.1469548.

Badawi, M., Abdelatif, M., Shebl, A., Makroum, F., Shalaby, A., Nemeth, N., 2022. Mapping Structurally Controlled Alterations Sparked by Hydrothermal Activity in the Fatira-Abu Zawal Area, Eastern Desert, Egypt. Acta Geol. Sin. - English Ed. https://doi.org/10.1111/1755-6724.15019.

Badawi, M.A., Makroum, F.M.A., Shalaby, A., Nemth, N., 2021. Geology and petrography of Mubarak area, central eastern desert, Egypt. Geosci. Eng. 9, 5–16. https://doi.org/10.33030/GEOSCIENCES.2021.14.005.

Carli, C., Sgavetti, M., 2011. Spectral characteristics of rocks: Effects of composition and texture and implications for the interpretation of planet surface compositions. Icarus 211, 1034–1048. https://doi.org/10.1016/J.ICARUS.2010.11.008.

Cooper, G.R.J., 2004. The textural analysis of gravity data using co-occurrence matrices. Comput. Geosci. 30, 107–115. https://doi.org/10.1016/J.CAGEO.2003.08.001.

Dentith, M., 1995. Textural filtering of aeromagnetic data. Explor. Geophys. 26, 209–214. https://doi.org/10.1071/EG995209.

Eldosouky, A.M., Elkhateeb, S.O., 2018. Texture analysis of aeromagnetic data for enhancing geologic features using co-occurrence matrices in Elallaqi area, South Eastern Desert of Egypt. NRIAG J. Astron. Geophys. 7, 155–161. https://doi.org/10.1016/J.NRJAG.2017.12.006.

Ghosh, T., Hazra, S., Kumar Das, A., 2022. Potential of ALOS-2 PALSAR-2 StripMap data for lithofacies identification and geological lineament mapping in vegetated fold-thrust belt of Nagaland, India. Adv. Sp. Res. 69, 1840–1862. https://doi.org/10.1016/J.ASR.2021.09.007.

Haralick, R.M., 1979. Statistical and structural approaches to texture. Proc. IEEE 67, 786–804. https://doi.org/10.1109/PROC.1979.11328.

Harris, J.R., 1989. Clustering of gamma ray spectrometer data using a computer image analysis system. Stat. Appl. Earth Sci. Geol. Surv. Canada, Canada 19–31.

Helba, H.A., Khalil, K.I., Abou, N.M.F., 2001. Alteration patterns related to hydrothermal gold mineralizaition in meta-andesites at Dungash Area, Eastern Desert, Egypt. Resour. Geol. 51, 19–30. https://doi.org/10.1111/j.1751-3928.2001.tb00078.x.

Kirkland, L., Herr, K., Keim, E., Adams, P., Salisbury, J., Hackwell, J., Treiman, A., 2002. First use of an airborne thermal infrared hyperspectral scanner for compositional mapping. Remote Sens. Environ. 80, 447–459. https://doi.org/10.1016/S0034-4257(01)00323-6.

Kusky, T., Wang, J., Wang, L., Huang, B., Ning, W., Fu, D., Peng, H., Deng, H., Polat, A., Zhong, Y., Shi, G., 2020. Mélanges through time: Life cycle of the world's largest Archean mélange compared with Mesozoic and Paleozoic subduction-accretion-collision mélanges. Earth-Science Rev. https://doi.org/10.1016/j.earscirev.2020.103303.

Li, N., Frei, M., Altermann, W., 2011. Textural and knowledge-based lithological classification of remote sensing data in Southwestern Prieska sub-basin, Transvaal Supergroup, South Africa. J. African Earth Sci. 60, 237–246. https://doi.org/10.1016/J.JAFREARSCI.2011.03.002.

Lu, Y., Yang, C., Meng, Z., 2021. Lithology Discrimination Using Sentinel-1 Dual-Pol Data and SRTM Data. Remote Sens. 2021, Vol. 13, Page 1280 13, 1280. https://doi.org/10.3390/RS13071280.

Lyon, R.J.P., 1965. Analysis of rocks by spectral infrared emission (8 to 25 microns). Econ. Geol. 60, 715–736. https://doi.org/10.2113/GSECONGEO.60.4.715.

Mahmoud, A., Elbialy, S., Pradhan, B., Buchroithner, M., 2011. Field-based landcover classification using TerraSAR-X texture analysis. Adv. Sp. Res. 48, 799–805. https://doi.org/10.1016/J.ASR.2011.04.005.

Mu, H.-X., Qiu, L., Yan, D.-P., Kong, R.-Y., Yang, W.-X., Gong, L.-X., Sun, P.-K., 2020. Spectral characteristics of hydrocarbon-bearing materials in Karamay, northwest China: implications for remote detection of onshore oil seeps. Spectrosc. Lett. 53, 543–558.

Mu, H.-X., Liu, C., Xu, L.-X., Rui, X.-M., Li, P.-J., 2023. Onshore hydrocarbon seep detection using the GF-5 hyperspectral image: a case study in the Karamay area. NW China. J. Maps 19, 2186276.

Najafi, P., Navid, H., Feizizadeh, B., Eskandari, I., 2018. Object-based satellite image analysis applied for crop residue estimating using landsat OLI imagery. International Journal of Remote Sensing 39, 6117–6136. https://doi.org/10.1080/01431161.2018.1454621.

Pour, A.B., Park, T.Y.S., Park, Y., Hong, J.K., Zoheir, B., Pradhan, B., Ayoobi, I., Hashim, M., 2018. Application of multi-sensor satellite data for exploration of Zn-Pb sulfide mineralization in the Franklinian Basin. North Greenland. Remote Sens. 10, 1186. https://doi.org/10.3390/rs10081186.

Pradhan, B., Hagemann, U., Shafapour Tehrany, M., Prechtel, N., 2014. An easy to use ArcMap based texture analysis program for extraction of flooded areas from TerraSAR-X satellite image. Comput. Geosci. 63, 34–43. https://doi.org/10.1016/J.CAGEO.2013.10.011.

Qiu, J.-T., Li, P.-J., Yu, Z.-F., Li, P., 2015a. Petrology and spectroscopy studies on danxia geoheritage in southeast Sichuan area, China: Implications for Danxia surveying and monitoring. Geoheritage 7, 307–318. https://doi.org/10.1007/s12371-015-0160-1.

Qiu, J.-T., Zhang, C., Hu, X., 2015b. Integration of concentration-area fractal modeling and spectral angle mapper for ferric iron alteration mapping and uranium exploration in the Xiemisitan Area. NW China. Remote Sens. 7, 13878–13894. https://doi.org/10.3390/rs71013878.

Qiu, J.-T., Mu, H.-X., Rui, X.-M., Yang, Y.-J., Li, P., Qiu, L., Xu, C.-B., 2024. The relationships between Danxia geoheritages and regional tectonics in southern Sichuan Basin: implications for the spatial distribution of Danxia landforms in China. Geoheritage 16, 24. https://doi.org/10.1007/s12371-024-00928-y.

Radford, D.D.G., Cracknell, M.J., Roach, M.J., Cumming, G.V., 2018. Geological Mapping in Western Tasmania Using Radar and Random Forests. IEEE J Sel. Top. Appl. Earth Obs. Remote Sens. 11, 3075–3087. https://doi.org/10.1109/JSTARS.2018.2855207.

Shakya, A.K., Ramola, A., Kandwal, A., Prakash, R., 2019. Change over time in grey levels of multispectral landsat 5^{TM}/8OLI satellite images. Lect. Notes Electr. Eng. 556, 309–356. https://doi.org/10.1007/978-981-13-7091-5_29/COVER.

Shebl, A., Csámer, Á., 2021b. Lithological, structural and hydrothermal alteration mapping utilizing remote sensing datasets: a case study around Um Salim area. Egypt. IOP Conf. Ser. Earth Environ. Sci. 942, 012032 https://doi.org/10.1088/1755-1315/942/1/012032.

Shebl, A., Csámer, Á., 2021c. Reappraisal of DEMs, Radar and optical datasets in lineaments extraction with emphasis on the spatial context. Remote Sens. Appl. Soc. Environ. 24, 100617 https://doi.org/10.1016/J.RSASE.2021.100617.

Shebl, A., Abdellatif, M., Hissen, M., Ibrahim Abdelaziz, M., Csámer, Á., 2021. Lithological mapping enhancement by integrating Sentinel 2 and gamma-ray data utilizing support vector machine: A case study from Egypt. Int. J. Appl. Earth Obs. Geoinf. 105, 102619 https://doi.org/10.1016/J.JAG.2021.102619.

Shebl, A., Csámer, Á., 2021a. Stacked vector multi-source lithologic classification utilizing machine learning algorithms: data potentiality and dimensionality monitoring. Remote Sens. Appl. Soc. Environ. 100643 https://doi.org/10.1016/J.RSASE.2021.100643.

Shebl, A., Kusky, T., Csámer, Á., 2022. Advanced land imager superiority in lithological classification utilizing machine learning algorithms. Arab. J. Geosci. 159 (15), 1–13. https://doi.org/10.1007/S12517-022-09948-W.

Shih, H.C., Stow, D.A., Chang, K.C., Roberts, D.A., Goulias, K.G., 2021. From Land cover to land use: applying random forest classifier to landsat imagery for urban land-use change mapping. Geocarto International 37, 5523–5546. https://doi.org/10.1080/10106049.2021.1923827.

Tassi, A., Vizzari, M., 2020. Object-oriented LULC classification in Google earth engine combining SNIC, GLCM, and machine learning algorithms. Remote Sens. 12, 3776. https://doi.org/10.3390/RS12223776.

Vaughan, R.G., Hook, S.J., Calvin, W.M., Taranik, J.V., 2005. Surface mineral mapping at Steamboat Springs, Nevada, USA, with multi-wavelength thermal infrared images. Remote Sens. Environ. 99, 140–158. https://doi.org/10.1016/J.RSE.2005.04.030.

Woodcock, C., Harward, V.J., 2007. Nested-hierarchical scene models and image segmentation. International Journal of Remote Sensing 13, 3167–3187. https://doi.org/10.1080/01431169208904109.

Zaini, N., Van Der Meer, F., Van Der Werff, H., 2012. Effect of grain size and mineral mixing on carbonate absorption features in the SWIR and TIR wavelength regions. Remote Sens. 4, 987–1003. https://doi.org/10.3390/RS4040987.

Zoheir, B., Weihed, P., 2014. Greenstone-hosted lode-gold mineralization at Dungash mine, Eastern Desert, Egypt. J. African Earth Sci. 99, 165–187.

Zoheir, B., El-Wahed, M.A., Pour, A.B., Abdelnasser, A., 2019. Orogenic gold in transpression and transtension zones: field and remote sensing studies of the barramiya–mueilha sector, Egypt. Remote Sens. 11, 2122.